

**Bio-optical properties and ocean color algorithms for coastal waters influenced by
the Mississippi River during a cold front passage.**

Eurico J. D'Sa, Richard L. Miller, and Carlos Del Castillo

E.J. D'Sa (ejdsa@lsu.edu) is with the Coastal Studies Institute, Department of Oceanography and Coastal Sciences, Louisiana State University, 306 Howe-Russell Geosciences Complex, Baton Rouge, LA 70803. R. L. Miller, and C. Del Castillo are with the Applied Sciences Directorate, NASA, Stennis Space Center, MS 39529.

Abstract

During the passage of a cold front in March 2002, bio-optical properties examined in coastal waters impacted by the Mississippi River indicated westward advective flows and increasing river discharge containing a larger nonalgal particle content contributed significantly to surface optical variability. A comparison of seasonal data from three cruises indicated spectral models of absorption and scattering to be generally consistent with other coastal environments, while their parameterization in terms of chlorophyll *a* concentration (Chl) showed seasonal variability. The exponential slope of the colored dissolved organic matter (CDOM) averaged $0.0161 \pm 0.00054 \text{ nm}^{-1}$, and for nonalgal absorption it averaged 0.011 nm^{-1} with deviations from general trends observed due to anomalous water properties. Although the phytoplankton specific absorption coefficients varied over a wide range (0.02 to $0.1 \text{ m}^2(\text{mg Chl})^{-1}$) being higher in offshore surface waters, values of phytoplankton absorption spectra at the SeaWiFS wavebands were highly correlated to modeled values. The normalized scattering spectral shapes and the mean spectrum were in agreement to observations in other coastal waters, while the backscattering ratios were on average lower in phytoplankton dominated surface waters (0.0101 ± 0.002) and higher in near-bottom waters (0.0191 ± 0.0045) with low Chl. Average percent differences in remote sensing reflectance R_{rs} derived from modeled and in-water radiometric measurements were highest in the blue wavebands (52%) and at sampling stations with a more stratified water column. Estimates of Chl and CDOM absorption derived from SeaWiFS images generated using regional empirical algorithms were highly correlated to in situ data.

OCIS codes: 010.4450, 290.1350, 120.0280.

1. Introduction

The Mississippi River (MR) system being one of the top 10 rivers in length, freshwater discharge, and sediment delivery¹, strongly influences primary productivity and carbon fluxes in the Northern Gulf of Mexico². The large spatial and temporal variations in biogeochemical processes occurring in these river dominated coastal margins coupled with large seasonal variability of freshwater discharge, coastal circulation and effects of frontal passages or storms have contributed to general uncertainties in the knowledge of oceanic fluxes of organic and inorganic matter to the shelf and open ocean waters.³ Satellite remote sensing with its capability for synoptic and repeated coverage of coastal waters has been found useful for monitoring many coastal processes. Ocean color remote sensing has been used to obtain estimates of phytoplankton biomass, colored dissolved organic matter (CDOM), water clarity, primary productivity and for tracing oceanic circulation features useful for carbon cycle studies.^{4,5} In recent years, occurrence of hypoxia or low dissolved oxygen concentration in the Louisiana coastal waters have been associated with high primary production and algal blooms due to enhanced nutrient concentrations in waters discharged by the MR.^{2,6} Reliable monitoring of these algal blooms will require improved knowledge of the optical characteristics of seawater constituents, and better optical models relating seawater constituents to the inherent optical properties (IOPs) of absorption and backscattering and the apparent optical properties (AOPs) such as remote sensing reflectance R_{rs} .

Empirical and semianalytic algorithms have been developed to obtain estimates of oceanic constituents and optical properties from ocean color data or remotely sensed reflectance data. These algorithms appear to perform well in oceanic Case 1 waters where

phytoplankton and its derived material are the main constituents determining ocean color,⁷ while their performance has been less than satisfactory in many optically complex Case 2 waters where other constituents (e.g., CDOM, detrital material or suspended sediments) are present and may not covary with chlorophyll *a* concentrations (Chl).^{8,9} Empirical algorithms use statistical relationships to link measured reflectance ratios to Chl,¹⁰ while semianalytic algorithms use a combination of equations derived using radiative transfer theory and empirical relationships (e.g., parameterization of the absorption coefficients in terms of Chl) to provide linkages between the AOPs such as reflectance, the IOPs (e.g., absorption and scattering) and seawater constituents.¹¹ Development of semianalytic algorithms have allowed for a greater number of variables (e.g., Chl, CDOM absorption) to be determined from remotely sensed ocean color satellite data^{5,12,13} and have been mainly applicable in Case 1 waters where Chl is the main variable influencing optical properties. Using an approach similar to Case 1 waters, studies have also addressed the application of empirical and semianalytic solutions to coastal waters including river impacted coastal systems,^{8,9,14,15} where for example,¹⁶ a linear relationship was shown to exist between the IOPs (absorption, backscattering) and the AOPs (diffuse attenuation coefficient, reflectance) in waters impacted by the seasonal MR discharge. Physical processes such as cold fronts and wind induced coastal circulation^{17,18} can further influence biogeochemical processes in the northern Gulf of Mexico. Frequent outbreaks of cold fronts in the winter months (generally from October to April) have been shown to affect water column physical properties (e.g., deepening of mixed layer) and air sea heat fluxes due to drier and colder air mass over the oceanic waters.^{19,20}

While these physical influences (frontal systems, wind induced coastal circulation) have been studied with respect to plume dynamics, physical effects and air-sea interaction, their influence on the bio-optical properties and remote sensing algorithms have not been addressed and is largely unknown. A field bio-optical study in waters impacted by the MR that coincided with the passage of a cold front and strong westward circulation currents allowed us to examine their effects on bio-optical properties, and remote sensing semianalytic and empirical algorithms. Using an approach similar to that for Case 1 waters, we examined the various parameterizations of the IOPs (absorption and scattering) in terms of Chl, and the correlations between radiometric derived R_{rs} and those derived from field measurements of IOPs. Further, we evaluated seasonal variability (April and October 2000, and March 2002) in optical properties to obtain a better understanding of the role of various seawater constituents (e.g., phytoplankton, detrital or nonalgal particles, and CDOM) on the optical properties and ocean color algorithms in an optically complex river dominated coastal environment.

2. Data and Methods

A. Study site and sampling strategy

The study site (Fig. 1) located on the Louisiana shelf in the Northern Gulf of Mexico is a region most directly influenced by the discharge from the MR. The MR enters the Gulf mainly through the birdsfoot delta through three large passes; the largest of which is Southwest (SW) Pass, followed by South Pass and East Pass. A seasonal river discharge and generally westward flowing alongshelf currents¹⁷ results in a major region of freshwater influence along the coast of Louisiana and Texas. Frontal passages (between

months of October and April) associated with cold air outbreaks often pass through coastal Louisiana with characteristic time scales of 3 to 10 days.²⁰

Sampling was conducted aboard the R/V Pelican from 17 to 26 March 2002 (high discharge period) that coincided with the passage of a frontal system. Twelve stations were occupied during the cruise aligned along three North-South transects (Fig. 1) that extended from shallow (~ 8 meters) coastal waters to offshore stations on the continental shelf. To examine the influence of physical processes (frontal passage and coastal circulation), the data were partitioned into measurements taken before (17-21 March) and after (23-26 March) the frontal passage. All 12 stations were occupied before the frontal passage while all but stations 9 and 11 were occupied after the frontal passage. At each station, water column optical and hydrographic measurements were made using a bio-optical instrumentation package and a CTD instrument. Water samples were taken at discrete depths (usually three) using Niskin bottles and processed onboard the ship or later in the laboratory. Atmospheric conditions during the cruise were obtained from a NOAA National Data Buoy Center C-MAN station located near the SW Pass (Fig. 1).

B. Hydrographic and bio-optical profile measurements

A vertical profiling bio-optical package comprising of a CTD (SBE 49, Sea-bird Electronics) and a suite of optical instruments enabled simultaneous measurements of water column optical (absorption, scattering, backscattering, chlorophyll fluorescence) and physical (temperature, salinity) variables. A data acquisition system (DH4, WET Labs) was used to acquire and archive data collected from all instruments in the bio-optical package and subsequently transfer data to a personal computer. Time-stamped

data from these instruments were aligned to CTD depth and vertical profiles were binned at either 0.5 m (shallow water stations) or 1.0 meter depth intervals. Profiles of chlorophyll fluorescence obtained using a flow through fluorometer (Wetstar, WET Labs) were converted to chlorophyll profiles by comparing High-Performance Liquid Chromatography (HPLC) Chl pigment estimates at discrete depths to fluorescence values at the same depths²¹ and are based on the assumption of a constant quantum fluorescence yield.^{22,23} Absorption and scattering coefficients at nine 10-nm spectral bands (412, 440, 488, 510, 532, 555, 650, 676, and 715 nm) were determined using a 25-cm dual path-length absorption and attenuation meter (ac-9, WET Labs). Using optically clean water as a reference (obtained from daily calibration of the ac-9 during the cruise), profiles of absorption and attenuation were corrected for temperature, salinity and scattering^{24,25} to give absorption a_{pg} (particulate absorption a_p plus a_{cdom}) and attenuation coefficients c . Particulate scattering b_p was determined as the difference of attenuation and absorption coefficients for all wavebands. Vertical profiles of absorption coefficients due to CDOM a_{cdom} were obtained by attaching a 0.2 μm pleated maxicapule filter (Gelman) to the intake tubing of the ac-9 during a separate cast at each station.

Vertical profiles of backscattering coefficients at three wavebands (450, 532 and 650 nm) were estimated using a factory calibrated²⁶ backscattering meter (VSF-3, WET Labs) from measurements of optical scattering at three angles of 100, 125, and 150° at each waveband. The relationship of backscattering coefficient b_b to the volume scattering function (VSF denoted by $\beta(\theta)$) through its integral in the backward direction²⁷ is used to determine the particulate backscattering coefficient b_{bp} at three wavebands from field measurements of particulate β_p ($\beta_p(100^\circ)$, $\beta_p(125^\circ)$, and $\beta_p(150^\circ)$) respectively. The

measured $\beta_p(\theta)$ values were corrected for light loss due to absorption over the pathlength at each angle and wavelength using the ac-9 data.²⁸ Further, a third-order polynomial was fitted through the three measured angles ($2\pi\beta_p(\theta)\sin\theta$) plus a fourth angle $\theta = \pi$, where $\beta_p(\pi)\sin\pi = 0$. Particulate backscattering coefficient b_{bp} at each of the three wavelengths were then determined by integrating the area under the polynomial.

Remote sensing reflectance R_{rs} (sr^{-1}) was determined from vertical profiles of downwelling irradiance $E_d(\lambda, z)$ ($\text{W m}^{-2} \text{nm}^{-1}$) and upwelling radiance $L_u(\lambda, z)$ ($\text{W m}^{-2} \text{nm}^{-1} \text{sr}^{-1}$) at seven 10-nm wavebands (412, 443, 490, 510, 555, 665 and 683 nm) using the OCI and OCR-200 radiometers (Satlantic). Dark values at these wavebands were obtained from night casts of the bio-optical package and were found to be relatively small for the downwelling irradiance ($\sim 0.3 \text{ W m}^{-2} \text{nm}^{-1}$) and upwelling radiance ($\sim 0.1 \text{ W m}^{-2} \text{nm}^{-1} \text{sr}^{-1}$) sensors, respectively. Spectral attenuation coefficients K_d and K_L were determined as the negative slope of $\ln E_d$ or L_u versus depth. An 11-point moving linear regression of $\ln E_d$ or L_u versus depth was used to obtain vertical profiles of K_d and K_L . Using values of K_d and K_L calculated at the shallowest measured depths, the values of $E_d(\lambda, 0^-)$ and $L_u(\lambda, 0^-)$ were estimated just beneath the sea surface. These subsurface values were extrapolated to values just above the sea surface $E_d(\lambda, 0^+)$ and $L_u(\lambda, 0^+)$ using known values of Fresnel reflectance at the water-air interface (1.04, 0.54)^{10,29} and were not adjusted for winds or sea state. R_{rs} was then calculated as

$$R_{rs} = L_u(\lambda, 0^+) / E_d(\lambda, 0^+). \quad (1)$$

In addition to the in-water derived values of R_{rs} , remote sensing reflectance was also determined from above-water measurements. Measurements of sky radiance and reflected radiance from the water surface and from a plaque with known spectral directional

reflectance (10 % spectralon, Labsphere) were made from the ship deck using a fiber-optic based high resolution spectral radiometer (GER 1500, Geophysical and Environmental Research) following SeaWiFS protocol and data processed for determination of above-water R_{rs} .^{29,30}

SeaWiFS ocean color data were obtained from Goddard Distributed Active Archive Center (DAAC) and processed using NASA's SeaDAS (version 4.8) software for estimating Chl using the OC4v4 algorithm and for R_{rs} using the Standard SeaWiFS atmospheric correction³¹ and the near infrared iterative method.³²

C. Discrete water sample analysis

Water samples at discrete depths at each of the sampling stations were collected using a CTD rosette multi-bottle array (General Oceanic Model 1015) immediately prior to or following optical profiles and samples either processed at sea or taken to the laboratory for various types of analyses (e.g., pigment concentrations, particulate and CDOM absorption spectra). Filtered samples (one each for each depth at a station) were stored in liquid nitrogen and processed later in the laboratory for pigments and spectral absorption within six months of sample collection. Phytoplankton pigment concentrations were determined using the HPLC method³³ following standard recommended SeaWiFS protocol.²⁹ while total particulate a_p and detrital or nonalgal absorption a_{nap} were determined using the quantitative filter pad technique (QFT).^{34,35} Phytoplankton absorption a_{ph} was then calculated as the difference between a_p and a_{nap} . Spectral absorption of CDOM was determined at sea by first filtering seawater samples through pre-rinsed 0.2 μm Nuclepore membrane filters followed by absorption measurements

using a multiple pathlength aqueous capillary waveguide based spectrophotometer^{36,37} within three hours of sample collection. S_{cdom} was then calculated as the slope of the log of the CDOM spectral absorption between 370 and 500 nm. Suspended particulate matter (SPM) concentration (mg l^{-1}) was determined gravimetrically using standard procedures.³⁸

D. Bio-optical Modeling

Models based on numerical simulations of underwater radiative transfer have been developed to relate AOPs such as subsurface irradiance reflectance $R(\lambda, \theta)$ or the above water spectral remote sensing reflectance R_{rs} to IOPs such as absorption $a(\lambda)$ and backscattering $b(\lambda)$ coefficients (m^{-1}) of the medium through the approximation^{11,27}

$$R_{rs} = 0.54 (f/Q) \times b_b / (a + b_b) \quad (2)$$

where the value 0.54 accounts for the Fresnel reflectivities at the sea surface, f is a parameter that depends upon the solar zenith angle, the optical properties of seawater, and Q is a factor that relates subsurface upwelling irradiance to the nadir upwelling radiance (sr) (just beneath the surface) and are both wavelength dependent.³⁹ The value of the ratio f/Q has been shown to vary less than f and Q individually for oceanic waters^{39,40} and were determined from field observations made in April of 2000.¹⁶ These values were found to be 0.103, 0.109, 0.114, 0.110, 0.105, 0.101, 0.09, and 0.089 sr at the SeaWiFS wavebands of 412, 443, 490, 510, 532, 555, 650, and 676 nm, respectively. The absorption $a(\lambda)$ and backscattering $b(\lambda)$ coefficients (Eq. 2) are the sum of contributions by the various seawater particulate and dissolved constituents including pure water. Knowledge of the spectral IOP characteristics of the various seawater components

(phytoplankton, detrital or nonalgal particles, and CDOM), and their parameterization in terms of Chl have been used in bio-optical models to extract information (e.g., concentration of seawater constituents, IOPs) from ocean color data or R_{rs} .^{5,11,41}

The total absorption coefficient a (m^{-1}) is the additive sum of contributions by pure water a_w ,⁴² phytoplankton a_{ph} , detrital or nonalgal particles a_{nap} , and CDOM absorption a_{cdom} and can be written as

$$a(\lambda) = a_w(\lambda) + a_{ph}(\lambda) + a_{nap}(\lambda) + a_{cdom}(\lambda). \quad (3)$$

In modeling total absorption in terms of Chl, phytoplankton absorption $a_{ph}(\lambda)$ has generally been expressed in terms of chlorophyll-specific absorption coefficient $a^*_{ph}(\lambda)$ ($m^2 \text{ mg Chl}^{-1}$) as

$$a_{ph}(\lambda) = a_{ph}(440) a^*_{ph}(\lambda), \quad (4)$$

with $a^*_{ph}(\lambda)$ spectra having the $a_{ph}(440)$ -normalized spectral shape and $a_{ph}(440)$ related to Chl through power law relationship given by⁴³

$$a_{ph}(440) = 0.0403[Chl]^{0.668}. \quad (5)$$

However, variability in $a^*_{ph}(\lambda)$ has been shown to exist for different regions,^{43,44} between species,³⁵ and within species due to changes in growth irradiance and pigment packaging effects.³⁵ In a different approach, given $a_{ph}(440)$, the $a_{ph}(\lambda)$ spectrum was modeled using the empirical relationship of Lee et al.⁴⁵ expressed as

$$a_{ph}(\lambda) = \{a_0(\lambda) + a_1(\lambda) \ln[a_{ph}(440)]\} a_{ph}(440), \quad (6)$$

where the values for $a_0(\lambda)$ and $a_1(\lambda)$ were empirically determined at 10 nm interval between 390 and 720 nm. The $a_{ph}(\lambda)$ spectrum can thus be determined using Eq. (6)

given a value of $a_{ph}(440)$ that can be obtained from Chl. In this study we examine both approaches to determine a more appropriate model for the study region.

With both CDOM and detrital spectral absorption exhibiting an exponential decrease in absorption with increasing wavelength, bio-optical models^{5,41} have generally combined the contribution by the two seawater constituents to the absorption field using values for slope of the log-linearized absorption coefficient S in the range 0.014 to 0.020. These have been fitted to the model

$$a_{cdom+nap}(\lambda) = a_{cdom+nap}(\lambda_0)e^{[-S(\lambda-\lambda_0)]}, \quad (7)$$

where $a_{cdom+nap}(\lambda_0)$ the absorption at a reference wavelength (generally between 400 and 440 nm) is then related to Chl.⁴⁶ In this study we examine the slopes S_{cdom} and S_{nap} of CDOM and nonalgal particle absorption coefficients separately using Eq. 7 to assess the appropriateness of using a single slope value in bio-optical models for the study region.

The total spectral scattering coefficient $b(\lambda)$ (m^{-1}) can be separated into contributions by pure water b_w ⁴⁷ and total particulate b_p as

$$b(\lambda) = b_w(\lambda) + b_p(\lambda). \quad (8)$$

With the backscattering coefficient being the term used in Eq. (2), it has, until recently, been a difficult parameter to measure directly. As such, particulate scattering b_p has been related to particulate backscattering b_{bp} through the backscattering ratio ($B = b_{bp}/b_p$), and the backscattering coefficient expressed as¹¹

$$b_b(\lambda) = \frac{1}{2} b_w(\lambda) + B b_p(\lambda). \quad (9)$$

A constant value generally used for the backscattering ratio ($B = 0.0183$) was determined from field measurements conducted in both coastal and oceanic waters.^{48,49} Further, particulate scattering has been generally parameterized in terms of Chl as⁵⁰

$$b_p(\lambda) = 0.416[Chl]^{0.766} (550/\lambda). \quad (10)$$

The spectral models for the IOPs and their parameterization in terms of Chl as described above have allowed the determination of seawater constituents and IOPs from ocean color or R_{rs} data mainly in Case 1 waters where phytoplankton and their derived products dominate the optical field. Other regional parameterizations of the IOPs have looked for similar dependence of absorption and scattering coefficients to Chl.⁴⁶ Here we take a similar approach in examining the spectral characteristics of the IOPs and their relationship to Chl in efforts to develop bio-optical models for river dominated waters where Chl concentrations are often high and could play a major role in influencing optical properties.

3. Results and Discussion

A. Atmospheric conditions, circulation features, and surface water properties

Prevailing winds in the MR delta region during March 2002 were easterly, southeasterly and have been shown to result in wind-driven currents that are primarily westward.⁵¹

These easterly winds are generally perturbed in winter (October to March) by frequent cold front passages that change the direction of the wind field from southeast to southwest, northwest, and northeast (Fig. 2). Relatively warm air temperatures ($\sim 22^\circ \text{C}$) with prevailing southeasterly winds ($\sim 6 \text{ m/s}$) during the prefrontal phase rapidly changed with the frontal passage to northerly winds ($\sim 15 \text{ m/s}$) resulting in a high pressure (1026 mbar), cold air ($\sim 10^\circ \text{C}$) system occupying the study region. By 23 March, wind speeds were back to about 6 m/s although the cold air occupied the region for another 24 hours before rising again.

Based on the general easterly, southeasterly winds in the region, westerly circulation currents were expected⁵² and also observed in the region from ADCP measurements (not shown). SeaWiFS Chl images (Fig. 3a, b, c, and d) documents the synoptic Chl pigment distribution before the frontal passage (17, 19 March), during the frontal passage (22 March), and after the frontal passage (24 March). These satellite images reveal the plume structure associated with higher Chl around the delta (Fig. 3a) and its intensification (Fig. 3b) due to in situ growth. Before the frontal passage, higher concentrations of algal biomass associated with discharge from the SW, South and East Pass were concentrated around the delta (Figs. 3a, b) and extended south up to about 28.5° latitude into the Gulf of Mexico. High Chl associated with increasing river discharge from SW Pass (Fig. 2c) were observed in the satellite Chl images of 22 and 24 March (Fig. 3c, d) along with a separate S-shaped band of high Chl that extended from the nearshore (st. 8) to the outer shelf (approximately 28.5° south latitude) showing patterns of westward displacement. Previous studies⁵¹ have documented a similar westward flow of plume waters turning anticyclonically northwestward towards the coast and have been attributed to the combined effects of volume discharge, winds, and the Coriolis force.⁵³

Cross-shelf transects through stations 8, 7, 6, and 5 on 18 and 24 March 2002 (Fig. 4) provided spatial and temporal information on near-surface (~ 2m depth) bio-physical properties of temperature, salinity and chlorophyll fluorescence (obtained from the ship-based flowthrough system with a CTD and fluorometer) associated with physical processes in the region. Surface salinity on the cross-shelf transect on 18 March 2002 (Fig. 4a) was relatively low (about 30.5 psu) except over a broad swath near st. 6 where it increased to about 32 psu. Phytoplankton biomass as indicated by the Chl fluorescence

signal varied from around 10 to 40 RFU (relative fluorescence units) and was lowest in higher salinity waters. SST was also variable and varied in concert with salinity, being higher or lower with salinity. Salinity through the same transect on 24 March after the frontal passage was lower and more variable than on 18 March, indicating the coastal current transport of river plume waters across the transect (Fig. 4b). Temperature followed a similar pattern as that of salinity and generally decreased in lower salinity waters. The phytoplankton biomass was however highest near the offshore stations and lowest at the nearshore st. 8. A band (~ 5 km width) containing very high phytoplankton biomass (~ 120 RFU) was present between stations 5 and 6 and was almost six times greater than at the nearshore st. 8 (~20 RFU). The SeaWiFS Chl satellite imagery of 24 March helps explain much of this short-term temporal and spatial variability in surface Chl fluorescence including the high Chl band between sts. 5 and 6 which appears to be a part of the S-shaped band observed in Fig. 3c. Patterns in the synoptic SeaWiFS Chl images however may not appear similar to the fluorescence transect due to strong westward coastal currents (speeds of about 1 m s^{-1} were recorded by the ship-borne ADCP; not shown) and the 24-hours that was required to cover the transect between sts. 5 and 8.

B. Temporal changes in bio-optical properties

We examine the short-term temporal surface properties (e.g., seawater constituents, physical, and optical) in relation to the frontal passage or the coastal currents at stations along the mid-transect (sts. 8, 7, 6 and 5), and two offshore sts. 4 and 12 (Table 1) using data acquired from the optical profiling package and discrete water samples. These

surface properties were an average of the top three meters, or in the case of discrete sampling within two meters of the surface. In some instances, due to variability in surface density stratification, differences were observed in the values obtained from discrete water sampling and those averaged from profiles. We observed that along the mid-transect and at the near-shore sts. 8, 7 and 6, salinities decreased, with the greatest change (31.89 to 27.56 psu) occurring at st. 6. At the offshore sts. 5, 12 and 4, surface densities varied from a low of 20.8 to 24.1 kg m⁻³ mainly due to salinity increases associated with westward flowing currents moving oceanic waters over these stations. At the nearshore st. 8, SPM decreased while CDOM absorption increased slightly over the time period. An examination of absorption components at 443 nm indicated that percentage contribution by CDOM at this waveband increased from 37 to 64% over the six-day period.

The backscattering ratio ($B = b_{bp}/b_p$) has been linked to the size of the nonalgal particles⁵⁴ (detritus and minerals) and to the refractive index with higher values of B associated with particles of higher refractive index (e.g., inorganic particles), and lower values associated with lower refractive index particles such as phytoplankton biomass.^{28,55,56} We observed a general increase in B across the mid-transect (sts. 5, 6, 7, and 8), indicating a relative increase in the inorganic component, while at the two outer sts. 4 and 12, a decrease in B (at 532 nm) indicated a relative increase in phytoplankton biomass after the frontal passage. At st. 6, B increased from 0.0072 to 0.017, and was associated with a larger increase in b_{bp} (0.0069 to 0.056 m⁻¹) than b_p (0.962 to 3.350 m⁻¹). We observed that although Chl more than doubled, there was an order of magnitude increase in SPM concentrations indicating stronger correlations between phytoplankton biomass and b_p and SPM and b_{bp} , respectively. Similarly, while there was only a doubling

of $a_{ph}(443)$, we observed an order of magnitude increase in $a_{nap}(443)$ from 0.022 to 0.379 m^{-1} , indicating that $a_{nap}(443)$ is more directly correlated to SPM concentrations. The increase in B from 0.0072 to 0.017 also indicated the presence of higher concentrations of inorganic particles or smaller sized organic detrital particles transported by the coastal current after the frontal passage. High SPM concentrations at st. 6 also suggests that advective flows were able to transport large quantities of SPM over relatively large distances. A comparison of optical properties (absorption and scattering) at the three offshore stations 4, 5, and 12, shows the largest changes (decrease) occurred at st. 4 which appeared to be occupied by more oceanic waters (salinity increased from 29.84 to 34.35). Although we observed a decrease in both Chl (4.57 to 0.99 $mg\ m^{-3}$) and CDOM absorption (0.21 to 0.073 m^{-1}), a decrease in the backscattering ratio from 0.011 to 0.008 (mean for 26 surface samples 0.011 ± 0.003) suggests a greater organic matter component in these oceanic waters. However smaller increases in salinity at stations 5 and 12 were accompanied by smaller increases in the concentrations of seawater constituents and optical properties indicating river influences at these stations. The large variability in the IOPs, and concentrations of seawater constituents (Chl, CDOM, and SPM) could be explained in terms of a combination of factors such as river influences, coastal currents and biological influences such as growth.

Water column physical and bio-optical properties before and after the frontal passage at sts. 6 (Fig. 5) and 2, 4, 5, 10 and 12 (Fig. 6) further demonstrates temporal changes in bio-optical properties over a six-day period. A large decrease in water column density (lower salinity and temperatures) following the front (Fig. 5) at st. 6 was mainly due to advection of lower salinity plume waters. As observed in Fig. 5a, the surface mixed layer

extended to about 3 meters with σ_t then rapidly increasing from 22.2 to about 24.0 kg m^{-3} near 10 m depth. Further increases in density with depth to oceanic conditions could be mainly attributed to salinity increasing to 36.2 at about 38 m. In contrast, water column density on 24 March at the same location was much lower (19.2 kg m^{-3} at surface) due to mainly advective flows of lower salinity waters in the region. Higher surface Chl generally decreased with depth (from about 2.1 and 7.2 mg m^{-3} in the surface to 0.2 and 1.5 mg m^{-3} at 25 m depth) over the two periods. On March 18, backscattering ratio ($B = b_{bp}/b_p$) was a low of 0.0072 in the surface mixed layer (Chl and SPM values of 2.11 mg m^{-3} and 0.54 mg l^{-1} , respectively) (Fig. 5a) that increased with depth and decreasing Chl. Lower Chl ($<0.2 \text{ mg m}^{-3}$) and higher SPM (2.98 mg l^{-1}) at 38 m resulted in a backscattering ratio (B at 532 nm) of about 0.02 and could be mainly attributed to a higher mineral or detrital component in the particulate pool. Similar inverse relationship between Chl and B observed in Case 2 waters were attributed to increasing refractive index of particles in the water.⁵⁵ In contrast, on 24 March the backscattering ratio was uniformly high throughout the water column (~ 0.017) in spite of higher Chl in surface waters (5.90 mg m^{-3}) and could be attributed to the lower salinity plume waters containing relatively larger concentrations of mineral and detrital particles throughout the water column (e.g., SPM concentrations of 5.67 and 4.35 mg l^{-1} at surface and at 15 m depth). Although a plot of Chl/SPM ratio versus B (Fig. 7) shows a general increase in B with decreasing values of Chl/SPM ratios, in the case of station 6, B remained relatively constant in spite of Chl/SPM ratios decreasing from 1.27×10^{-3} at surface to 0.64×10^{-3} at 16 m. One possible explanation for the constant B profile is that with st. 6 being approximately 62 km to the west of SW Pass, the relatively high concentrations of SPM

would mainly comprise of smaller size mineral and detrital particles being transported over longer distances in suspension.

Higher concentrations of seawater constituents in the surface mixed layer were reflected in the higher values of IOPs (Figs. 5 and 6). Vertical profiles of CDOM absorption, particulate plus CDOM absorption and scattering were higher in surface waters and generally decreased with depth (Fig. 5c, d), with much higher values on 24 March. CDOM absorption (shown at 440 nm) more than doubled while particulate plus CDOM absorption and scattering were almost factor of three larger throughout the water column. An examination of vertical profiles of salinity, Chl and the optical properties of absorption and scattering and B at sts. 2, 4, 5, 10, and 12 (Fig. 6a-j) obtained before and after the frontal passage also shows lower surface salinity values and higher Chl and absorption and scattering in near surface waters with the largest increase in absorption and scattering observed at station 10. Vertical profiles of B (Fig. 6e and j) shows a general increase in B with increasing depth. Average surface values for all the stations were 0.0101 ± 0.002 while the average bottom values were 0.0191 ± 0.0045 before the frontal passage that increased slightly to 0.0193 ± 0.0057 after the frontal passage. Changes in B due to the relative influence of various seawater constituents (e.g., phytoplankton, suspended sediments, and detrital material) and their size variations suggests the need for better characterization of the seawater constituents and their optical properties. Examining such relationships between optical properties and the seawater constituents have the potential to provide useful information on bulk particulate composition and as a tracer of water movement^{28,55,56} in river-dominated coastal margins.

A seasonal comparison (April and October 2000, and March 2002) of CDOM absorption at 412 nm plotted as a function of salinity obtained from discrete water samples at different depths (Fig. 8a) shows an inverse relationship between CDOM absorption at 412 nm and salinity ($r^2 = 0.95$). In spite of the large seasonal river discharge during the three measurement periods (mean of 17,000, 5000 and 17,500 $\text{m}^3 \text{s}^{-1}$ respectively during April and October 2000 and March 2002) a conservative relationship is observed between CDOM absorption and salinity. High correlations are observed for CDOM absorption varying over two orders of magnitude in a study region that covered a larger area and seasonal river discharge in April and October of 2000 (see D'Sa and Miller 2003). A scatter plot of S_{cdom} (the slope parameter for the a_{cdom} spectral decay) as a function of $a_{cdom}(412)$ (Fig. 8b) shows as in some previous results⁵⁷ S_{cdom} decreasing with increasing a_{cdom} (or decreasing salinity) for the March 2002 period while we observe a much greater scatter for the April and October 2000 cruises. Contributions of instrument variability to the scatter cannot be discounted since CDOM absorption measurements for the spring and fall 2000 cruises were made using an initial version of the multi-pathlength waveguide and a spectrophotometer, respectively. Average S_{cdom} for April and October 2000, and March 2002 varied over a relatively narrow range and were 0.0151 ± 0.0017 , $0.0162 \pm 0.0018 \text{ nm}^{-1}$, and $0.0161 \pm 0.00054 \text{ nm}^{-1}$, respectively. A closer examination of values of both CDOM absorption and S_{cdom} for the March 2002 measurements revealed a few stations with possible different sources of CDOM or composition such as humic and fulvic acids.⁵⁷ Station 9 had CDOM absorption values that were lower than expected and was associated with outflow from the Barataria Bay (measured surface salinities were lower than nearby stations 10 and 8). In comparison to values of 0.016 nm^{-1} at stations 2

and 3 observed before the frontal passage, S_{cdom} values at these stations were 0.0149 and 0.0148 nm^{-1} on 26 March and may have been related to a different source of river water associated with the increasing river discharge (Fig. 2c). However, the largest observed variation in S_{cdom} (0.0141 nm^{-1}) occurred at station 6 (18 March, 38 m depth, salinity 36.14 psu) and appears to be associated with an anomalous water mass with slightly elevated Chl and scattering values (Fig. 6a, c).

C. Characteristics of absorption coefficients

IOPs and seawater constituents have been determined from inverse modeling of remote sensing reflectance using knowledge of the spectral characteristics of the surface water constituents and their relationships to Chl.^{5,13} We examined the spectral characteristics of particulate and dissolved surface seawater constituents (Fig. 9) and observed for example, a large range in the variability of spectral absorption values over a six-day period (pure water absorption shown for reference) for phytoplankton, CDOM and nonalgal absorption. For example in surface waters at station 6, phytoplankton and CDOM were the primary contributors to absorption before the frontal passage (Fig. 9a, a_{ph1} ; Table 1), while CDOM and nonalgal particle absorption (a_{cdom2} , a_{nap2}) formed a significant component of the total absorption after the frontal passage.

Phytoplankton absorption spectra obtained from surface samples at the sampling stations were highly variable and covered a large range at the blue (0.06 to 0.6 m^{-1}) and red (0.04 to 0.4 m^{-1}) absorption peaks (Fig. 9b, x-axis). Phytoplankton absorption spectra determined using the model of Lee et al.⁴⁵ with values of the constants $a_0(\lambda)$ and $a_1(\lambda)$ and Eq. 6 (at the SeaWiFS wavebands) were observed to be highly correlated to measured

phytoplankton spectra (Fig. 9b). However as observed in Fig. 9a (superimposed triangles and circles obtained using Eq. 6), the model fit at 555 nm waveband shows higher values than the actual a_{ph} spectra, and as such by reducing the values of the two constants by 0.0414 and 0.0061 (essentially using values of constants shifted up by 10 nm) we obtained a much improved fit ($r^2 = 0.97$; Fig. 9b) at this waveband for most a_{ph} spectra of surface samples taken in the study region.

Chlorophyll-specific phytoplankton absorption coefficient spectra a^*_{ph} of surface seawater samples (Fig. 9c) in the study area were observed to vary both spatially and temporally with variations in the blue and red absorption peaks of 0.02-0.1 and 0.02-0.09

$\text{m}^2(\text{mg Chl})^{-1}$, respectively. Highest values were observed at the offshore st. 5 for samples taken before and after the frontal passage and the lowest for stations directly influenced by the plume waters (sts. 2, 3, 6, 7, and 8). a^*_{ph} values for other stations were within those for sts. 2 and 5. Factors such as pigment packaging, nutrients, taxonomic changes, and photoadaptation have been attributed to a^*_{ph} variability in oceanic waters.^{35,43,58}

Many of these factors could have influenced a^*_{ph} variability in the study region which in conjunction with physical factors such as freshwater inputs, mixing and advection strongly influences primary productivity in the region.² Similar a^*_{ph} variability observed in other coastal waters⁵⁹ have important implications in the estimation of primary production from ocean color satellite data.

In Fig 9a, we observed that although both detrital or nonalgal particles and CDOM absorption decreased exponentially with increasing wavelength, they do so with different slopes. Although most semianalytic models have combined the contributions by these two seawater constituents (Eq. 7), we observed that these slopes are different, being on

average about 0.011 for nonalgal particles (Fig. 9d) and 0.016 nm⁻¹ for CDOM (Fig. 9f). The a_{nap} spectra of surface seawater samples followed the standard exponential decrease with increasing wavelength and the average slope compared well with those described in other coastal environments.^{59,60} However there was a wide range in the magnitude of a_{nap} absorption at 443 nm (0.019 to 0.892 m⁻¹) being highest at the station near the SW Pass and lowest at the outermost oceanic stations. Although the average S_{nap} slope was 0.011 nm⁻¹, it varied from 0.0085 to 0.0121 nm⁻¹ with the lowest values of 0.0085 and 0.0089 nm⁻¹ observed at the nearshore stations 9 (surface waters) and 8 (bottom) off the Barataria Bay suggesting waters with different particle composition or properties. Absorption by

nonalgal particles relative to total particulate absorption a_p at 443 nm (Fig. 9e) varied from about 10% at the outermost station 5 to about 85% for station 3 near the SW Pass and were in the range 10 to 30% for most near surface stations with chlorophyll concentrations between 2 to 6 mg.m⁻³. The slope of $a_{nap}:a_p$ versus Chl for stations sampled after the frontal passage appeared to be greater than those before the passage suggesting a greater nonalgal particle content in waters discharged by the Mississippi River after the frontal passage. Deviations were also observed in the CDOM spectral characteristics (Fig. 9f) where the CDOM absorption $a_{cdom}(412)$ varied from 0.04 in oceanic waters to 1.2 m⁻¹ near the river mouth while the slope S_{cdom} varied from 0.014 to 0.0178 nm⁻¹. These absorption properties suggest that near coastal waters with different freshwater sources potentially have optical properties different from surrounding water masses and the use of standard parameterizations may not be appropriate for these waters.

In examining the absorption by phytoplankton, nonalgal particles at 443 nm and CDOM at 412 nm in terms of Chl (Fig. 10a, b and c), we observe that both $a_{nap}(443)$ and

$a_{cdm}(412)$ were highly correlated ($r^2 > 0.9$) to Chl for the March 2002 data while the April and October 2000 data showed greater scatter. Lower correlations between $a_{ph}(443)$ and Chl ($r^2 = 0.74$) (Fig. 10a) for March 2002 data could be attributed to variability in surface Chl (standard deviation were ± 0.01 to 1.6 for Chl between 0.68 to 12.23 mg m⁻³) resulting in some differences between discretely sampled values and Chl averaged over the surface 3 m. Comparison to limited data of April 2000 indicates similar relationship for the two periods. The non-linearity observed between suspended particulate matter (SPM) and Chl (Fig. 10d) for March 2002 were similar to those between a_{nap} and Chl and could be attributed to the relatively large concentrations of nonalgal material (suspended sediments and detrital organic matter) at stations near the river. Strong currents observed at the study site ($>1\text{ m s}^{-1}$) may have carried large concentrations of SPM to distances such as those observed at st. 6. However a nonlinear relationship is not observed for the April and October 2000 measurements with SPM that were low due to low river discharge. We observe that the above parameterizations would not be applicable seasonally and also differed with those obtained from other studies,^{43,46} suggesting a better need to better evaluate seasonal absorption parameterizations for retrieving in-water constituents and optical properties.

D. Characteristics of scattering coefficients

Relative dominance from contributions by different particulate field (e.g., phytoplankton, suspended sediments, detritus) influenced the spectral scattering coefficients b_p which was highly variable (0.41 - 4.54 m⁻¹ at 440 nm; Fig 11b) and exhibited wavelength dependence that was rather small at lower absorption and increased at higher values (not

shown). Relatively different ratios of phytoplankton and nonalgal (suspended sediments and detrital) particles (Fig. 9e) before and after the frontal passage resulted in better correlations between phytoplankton and scattering before the frontal passage and between nonalgal particles and scattering after the frontal passage (not shown). River water discharge which increased dramatically after the frontal passage (Fig. 2c) appeared to contain higher concentration of nonalgal particles that were better correlated to scattering (not shown). The scattering spectral dependence has been previously shown to vary as λ^n with n generally having values from 0 to -2.^{11,61} To account for the varying shape of the scattering spectrum, we normalized the $b_p(\lambda)$ values with respect to the spectrally averaged scattering coefficient, $\langle b_p \rangle$ that was computed between the 412 and 715 nm.⁵⁹ Troughs observed in the normalized scattering spectra are due chlorophyll *a* absorption effects on scattering corresponding to the absorption maxima in the blue (around 440 nm) and red (676 nm) spectral region. The normalized spectral shapes appeared similar to those in other coastal waters⁵⁹ with larger troughs at stations with high Chl and almost flat at locations with low Chl concentrations. The mean spectrum for all the data (Fig. 11a, bottom panel) compared well with the linear relationship between $b_p(\lambda)$ and λ for observations that included the northern Gulf of Mexico⁴⁹ and is flatter than the typical value of -1 used for the power function λ^n to describe the shape of the scattering spectra.

Although a constant value (0.0183) has been often used for the backscattering ratio B ,^{48,49} a nonlinear relationship previously reported for the study region¹⁶ is being confirmed in this study (Fig. 9b). Water column profiles (Figs. 5a, b; 6e, j) and surface values of B at sampling stations (Table 1) confirm observations that B is not a constant in these waters, generally having lower values in phytoplankton dominated waters and

higher values in waters with higher concentrations of suspended sediments and indicative of the bulk refractive indices of the water. Increasing backscattering in relation to total scattering due to higher refractive indices in waters with higher suspended sediments or smaller sized nonalgal particles could be attributed to the observed non-linearity in the backscattering ratio. A comparison of the relationship between b_p and Chl used in inverse modeling (e.g., Eq. 10) indicates that in these river dominated waters the observed relationship is higher than those developed for case 1 waters (Fig. 11c).⁵⁰ As in other coastal waters⁴⁹ a seasonal comparison of the data (spring and fall 2000) also indicates values falling above the model line that can be attributed mainly to increased contribution to scattering by the suspended sediments or detrital particles.

E. Remote sensing reflectance: radiometric versus model derived

We compared the R_{rs} spectra for a set of representative stations derived from in-water radiometric measurements at the six visible SeaWiFS wavebands (412, 443, 490, 510, 555, and 670 nm) with those modeled from surface IOP estimates (absorption, scattering, and backscattering ratio) applied to Eq. 2 (Fig. 12). We observed both high and variable concentrations of both SPM and CDOM in the study region. In such waters the bi-directional f/Q function besides being dependent on the Sun-angle, can be influenced by both sediment and CDOM dominated waters or is simply unpredictable.⁶² However, we used the f/Q values obtained from a previous study in the region¹⁶ on the assumption that the range of variability of the ratio f/Q is narrower than f or Q individually,^{39,40} and the values could be typical for these coastal waters.

R_{rs} spectra were found to be variable in shape and exhibited characteristics associated with oceanic waters where Chl was the main seawater constituent (st. 12; Fig. 12, third row) to more coastal waters (sts. 6, 10, 11, 4, 7, and 8) where Chl, CDOM and suspended sediments all contributed to the reflectance field. The mean percent difference for all the stations shown in Fig. 12 (calculated as $100 \times (R_{rs-model} - R_{rs-insitu}) / 0.5(R_{rs-model} + R_{rs-insitu})$) was highest in the blue at 412 nm ($52 \pm 28\%$) and lowest ($-4 \pm 18\%$) at the 555 nm waveband. However, at stations with low R_{rs} values (e.g., st. 12 at 670 nm waveband) percent differences were large even though differences in absolute magnitude were small. Contributions by dissolved and nonalgal or detrital absorption significantly influenced R_{rs} in the blue waveband at some stations; while backscattering by phytoplankton and suspended sediments influenced ocean color in the green and red parts of the spectrum at other stations. CDOM absorption at 412 nm which varied from a low of 0.103 (at st. 12, sampled on 25 March) to a high of 0.417 m^{-1} at st. 7 along with phytoplankton absorption (with Chl varying from 0.68 at st. 12 to 6.11 mg m^{-3} at st. 7) contributed more than 70% to total absorption in the blue wavebands and determined the R_{rs} spectra with reflectance lower in the blue than the green wavebands. Relatively larger contribution ($\sim 30\%$) by nonalgal absorption (suspended sediments and detrital material) with SPM concentrations of 4.02 mg l^{-1} at st. 7 (bottom row) resulted in a large difference between the blue and green wavebands. The largest observed R_{rs} value (0.00918 sr^{-1}) at the 555 nm waveband could be attributed to the high $b_{bp}(532)$ value of 0.0312 m^{-1} measured at st. 7. The largest percent difference (107% in the blue and -40% in the red) between in-water and model derived R_{rs} at this station may be attributed to the strong stratification where a surface low salinity (27.2 psu) mixed layer (0-4 m) with high Chl (6.11 mg m^{-3}) and $a_{cdm}(412)$ of

0.416 m^{-1} overlay a higher salinity (30.3 psu) lower Chl (4.11 mg m^{-3}) and CDOM subsurface water mass (Fig. 6, lower panel). Ignoring subsurface contributions of IOPs used in deriving the model estimates or the complexity of the underwater light field may have resulted in the large differences at this station. At st. 12 (third row) low Chl (0.68 mg m^{-3}), CDOM (0.093 m^{-1}), SPM (0.98 mg l^{-1}) and backscattering $b_{bp}(532)$ (0.00536 m^{-1}) resulted in a shift of the peak in R_{rs} from 555 nm to around 490 nm. Larger differences between the in-water derived and model derived estimates of R_{rs} spectra in the blue could be attributed to the combined effects of higher light penetration in the blue and surface stratification, while stratification would have reduced effect in the red due to limited penetration of red light in the water. An examination of the vertical IOP profiles (e.g., Figs. 5, 6) indicated that the average surface (0 – 3 m) IOPs values used in deriving the R_{rs} spectra using Eq. 2 may not always have been representative of their effects on the radiance field. It appears that the highly stratified river dominated coastal waters with its non-uniform vertical bio-optical properties may have influenced both the radiometric and IOP derived estimates of R_{rs} . Smaller differences in R_{rs} spectra observed at higher wavebands at most stations suggest that the model derived estimates are well represented by the IOPs in the surface 3 m, while in the blue contributions by CDOM and phytoplankton at greater depths influenced the radiance field. Also, since the measurements were made at different times during the day the upward radiance field could still be non-isotropic and dependent on Sun's position in these coastal waters⁶² and the f/Q values used may not have been the most appropriate. Other factors such as the in-water radiometric measurement uncertainties associated with extrapolation of subsurface measurements to above-water values, shelf-shading, and in the case of modeled outputs,

to uncertainties in the scattering corrections for the ac-9 measured absorption and scattering coefficients⁶³ may have also contributed to the differences in R_{rs} spectra.

We also examined the SeaWiFS derived R_{rs} spectra for three nearshore sts. 7, 8, and 10 using the standard SeaWiFS atmospheric correction algorithm³¹ that assumes negligible water leaving radiance in the near infrared part of the spectrum and the iterative method³² that corrects for the non-negligible water reflectance in the near infrared in waters with chlorophyll concentrations greater than $\sim 2 \text{ mg m}^{-3}$. We observed that at st. 7, the R_{rs} spectra derived from SeaWiFS data using the two methods differed across the spectrum and had larger differences in the blue wavebands. The standard

atmospheric correction algorithm compared well with the in-water derived R_{rs} in the blue

with both having low values due high absorption by CDOM, Chl and nonalgal or detrital

particles, while the iterative algorithm overestimated the spectral values in the blue. In

the case of st. 8, a more uniform near-surface (0 – 6 m) high Chl (4.04 mg m^{-3}) and

CDOM (0.312 m^{-1}) may have resulted in all the derived R_{rs} spectra matching closely

across the spectra. Both the SeaWiFS atmospheric correction algorithms correlated with

the in-water and model derived reflectance suggesting the atmospheric correction

algorithm to have worked well at this station. However at st. 10, R_{rs} derived from

SeaWiFS using both the atmospheric correction algorithms overestimated those derived

using the model and in-water measurements (Fig. 12, second row). Although surface Chl

(3.22 mg m^{-3}), CDOM absorption at 412 nm (0.29 m^{-1}) and SPM (3.76 mg l^{-1}) were

typical of other stations, observed subsurface Chl (4.7 mg m^{-3}) peak (Fig. 6; top row) at

about 8 m depth does not explain the differences between field and satellite estimates.

The results of these comparisons suggest both the potential and complexity in developing

semianalytic and IOP inversion models and their application in ocean color remote sensing in these coastal waters.

A comparison of R_{rs} spectra derived from above-water measurements with those modeled using IOPs and the in-water radiometric derived spectra show the above-water derived R_{rs} to have lower values across the spectra for all the stations. Better correlations between SeaWiFS, model and in-water derived R_{rs} (Fig. 12) suggest the above-water measurements may be biased due to environmental factors such as Sun angle, cloud cover, wind speed, or viewing geometry⁶³. However, an examination of R_{rs} spectra in the near-infrared (e.g., 670 nm) indicates the above-water R_{rs} to differ significantly from the other methods which appear to be in better agreement at this waveband. We note here that in deriving above-water R_{rs} using SeaWiFS protocol^{29,30} sky radiance is removed from the ocean radiance signal followed by the removal of any residual signal at 750 nm. The correction at 750 nm is based on the assumption that the water-leaving radiance at 750 nm is zero and that the reflected sky radiance has a white spectral shape.³⁰ It appears that the residual correction also removed a component of the water leaving signal in the near-infrared resulting in values of R_{rs} that were lower than those derived by other methods. Other factors such as environmental and viewing conditions could have contributed to uncertainties with above-water reflectance measurements. However, ease of measurements with the above-water radiometer has allowed for more routine use of this method in determinations of remote sensing reflectance for ocean color applications.

F. Empirical ocean color algorithms for Chl and CDOM

Although we observed differences in magnitude between in-water and above-water derived R_{rs} , a comparison of the ratios of R_{rs} used in ocean color algorithms (e.g., $R_{rs}(490)/R_{rs}(555)$, or $R_{rs}(510)/R_{rs}(555)$) for measurements made during three field cruises in the spring and fall of 2000 and March 2002 showed them to be highly correlated (Fig. 13a, b). Based on these results and using a more extensive set of remote sensing spectra derived from above-water radiometric measurements made during the three cruises, regression analysis of log-transformed reflectance ratio $R_{rs}(490)/R_{rs}(555)$ and Chl and the ratio $R_{rs}(510)/R_{rs}(555)$ and CDOM absorption (Fig. 13c, d) indicated high correlation between the $R_{rs}(\lambda)$ ratios and Chl ($r^2 > 0.8$) and CDOM absorption at 412 nm ($r^2 > 0.7$).

Power law equations for Chl and CDOM absorption derived from the regression analysis were determined as

$$\text{Chl} = 1.63(R_{rs}(490) / R_{rs}(555))^{-2.512} \quad (11)$$

$$a_{\text{cdom}}(412) = 0.227(R_{rs}(510) / R_{rs}(555))^{-2.022} \quad (12)$$

The $R_{rs}(490)/R_{rs}(555)$ reflectance band ratio algorithm for Chl and the $R_{rs}(510)/R_{rs}(555)$ band ratio for CDOM absorption have been shown to perform relatively well for the study region.¹⁶ Estimates of Chl and CDOM absorption obtained from SeaWiFS data using these empirical relationships show good agreement with a seasonal set of in situ data obtained in April and October of 2000 and March 2002 (Fig. 14). Although both seasonal and short-term effects were observed in the optical properties, the bio-optical relationships determined for these waters provided a sound basis for retrieval of these variables using the empirical algorithms.

4. Conclusion

We examined bio-optical properties in a large river-dominated environment during the passage of a frontal system in March 2002 that also coincided with westward circulation flows and an increasingly large discharge from the Mississippi River. Optical properties were also compared to seasonal data obtained in the spring and fall of 2000 that corresponded to a year when the discharge from the Mississippi River was very low.

SeaWiFS Chl images obtained before, during and after the frontal passage in March 2002 revealed high Chl around the delta, its intensification and subsequent westward displacement. Lower salinities observed during cross-shelf hydrographic measurements

after the frontal passage also indicated westward transport of plume waters. A combination of factors that included transport, in situ growth (observed in satellite image), and a large increase in river discharge influenced the spatial and temporal variability in seawater constituents and the optical properties. A relative increase in percentage of nonalgal absorption relative to algal absorption after the frontal passage was reflected on an average increase in the backscattering ratio (0.0074 to 0.014) at stations directly influenced by plume waters while at the offshore stations it remained low (0.0085). Non linearities observed between $a_{nap}(443)$ and SPM and Chl could be attributed to the high concentrations of nonalgal particles (suspended sediments and organic detrital material) at stations more directly influenced by river water. Similar correlations were however weak or nonexistent for the April and October cruises. The spectral absorption and scattering characterization of seawater constituents such as phytoplankton, CDOM and nonalgal particles were found to be similar to those determined for other coastal waters.^{37,49,59,60} We observed a non-linear relationship for the

backscattering ratio that can be attributed relative changes in particle composition. The observed short-term variability in algal to nonalgal absorption will relate to uncertainties in describing absorption in bio-optical models⁴¹ with consequences in obtaining reliable estimates of seawater constituents and optical properties from ocean color remote sensing.

A comparison of R_{rs} spectra derived from in-water radiometric measurements and those derived using the IOP model¹¹ indicated larger mean differences (52%) in the blue waveband where contributions by CDOM and phytoplankton absorption were most significant. There appeared to be a relative increase in the contribution by nonalgal absorption or backscattering⁶⁴ at some stations after the frontal passage associated with a large increase in river discharge. A combination of factors including deeper light penetration in the blue; water stratification, model derivation using only the near surface (0–3m) values of IOPs and instrument measurement uncertainties contributed to the relatively larger differences in the blue waveband. In contrast differences at higher wavebands (green and near-infrared) were relatively small (4%) due to the greater absorption of light by pure water and its penetration to shorter depths. A comparison of model and in-water derived R_{rs} spectra with those derived from SeaWiFS satellite data using the standard atmospheric correction algorithm and the iterative coastal algorithm indicated the best correlation to occur at a station with uniform near-surface Chl distribution while greater differences were observed at stations with stronger near surface stratification and non uniform vertical Chl distributions. This study has provided better insights into the variability of the ocean color reflectance measurements derived from both field and satellite data in relation to seawater constituents in an optically complex

river-dominated system. Estimates of Chl and CDOM absorption derived from SeaWiFS ocean color data using the regional empirical algorithms were found to be highly correlated to in situ measurements acquired during both high and low MR flows. In spite of a conservative relation observed between CDOM absorption and salinity for measurements presented in this and other studies,⁶⁵ results of this study indicate both short-term and seasonal variability in the bio-optical properties suggesting need for more studies and caution in the use of semianalytic algorithms for this complex river dominated coastal environment.

This study was supported by a NASA-EPSCoR grant involving Louisiana Marine Consortium (LUMCON), Tulane University, and NASA Stennis Space Center. The authors wish to thank Brent McKee (Tulane University) for the SPM data and the reviewers for very insightful comments and suggestions that greatly improved the manuscript. Partial support of this work is acknowledged from a NASA-EPSCoR grant (NASA/LEQSF(2005)-DART-17) to E. J. D'Sa.

References

1. J. D. Milliman, and R. H. Meade, "World-wide delivery of river sediment to the ocean. *J. Geology*, **91**, 1-21 (1983).
2. S. E. Lohrenz, G. L. Fahnenstiel, D. G. Redalje, G. A. Lang, X. Chen, M. J. Dagg, T. E. Whittedge, and Q. Dortch, "Nutrients, irradiance, and mixing as factors regulating primary production in coastal waters impacted by the Mississippi River," *Cont. Shelf Res.* **19**, 1113-1141 (1999).
3. R. Wollast, "The coastal organic carbon cycle: Fluxes, sources and sinks," in *Ocean margin processes in global change*, R.F. Mantoura, J.-M. Martin and R. Wollast, eds. (Wiley and Sons, 1991).
4. C. R. McClain, J. A. Yoder, L. P. Atkinson, J. O. Blanton, T. N. Lee, J. J. Singer, and F. Muller-Karger, "Variability of surface pigment concentrations in the South Atlantic Bight," *J. Geophys. Res.* **93**, 10675-10697 (1988).
5. K.L. Carder, K. L. R. F. Chen, Z. P. Lee, and S. K. Hawes, "Semianalytic moderate-resolution imaging spectrometer algorithms for chlorophyll *a* and absorption with bio-optical domains based on nitrate-depletion temperatures," *J. Geophys. Res.* **104**, 5403-5421 (1999).
6. N. N. Rabalais, R. E. Turner, and W. J. Wiseman, "Hypoxia in the Gulf of Mexico," *J. Environ. Qual.* **30**, 320-329 (2001).
7. A. Morel, and L. Prieur, "Analysis of variations in ocean color," *Limnol. Oceanogr.*, **22**, 709-722 (1977).
8. E. J. D'Sa, C. Hu, F. E. Muller-Karger, and K.L. Carder, "Estimation of colored dissolved organic matter and salinity fields in case 2 waters using SeaWiFS: Examples

from Florida Bay and Florida Shelf,” *Earth Planetary Sci. (Indian Acad. Sci.)* **111**, 197-207 (2002).

9. M. Darecki, and D. Stramski, “An evaluation of MODIS and SeaWiFS bio-optical algorithms in the Baltic Sea,” *Remote Sens. Environ.* **89**, 326-350 (2004).
10. J. E. O’Reilly, S. Maritorena, B. G. Mitchell, D. A. Siegel, K. L. Carder, S. A. Garver, M. Kahru, and C. McClain, “Ocean color algorithms for SeaWiFS,” *J. Geophys. Res.* **103**, 24937-24953 (1998).
11. H. R. Gordon, O. B. Brown, R. H. Evans, J. W. Brown, R. C. Smith, K. S. Baker, and D. K. Clark, “A semianalytic radiance model of ocean color,” *J. Geophys. Res.* **93**, 10909-10924 (1988).
12. Z. P. Lee, K. L. Carder and R. A. Arnone, “Deriving inherent optical properties from water color: a multiband quasi-analytical algorithm for optically deep waters,” *Appl. Opt.* **41**, 5755-5772 (2002).
13. S. Maritorena, D. A. Siegel, and A. R. Peterson, “Optimization of a semianalytical ocean color model for global-scale applications,” *App. Opt.* **41**, 2705-2714 (2002).
14. H. T. Hochman, F. E. Muller-Karger, and J. J. Walsh, “ Interpretation of the coastal zone color scanner signature of the Orinoco River plume,” *J. Geophys. Res.* **99**, 7443-7455 (1994).
15. B. Hamre, O. Frette, S. R. Erga, J. J. Stamnes, and K. Stamnes, “Parameterization and analysis of the optical absorption and scattering coefficients in a western Norwegian fjord: a case II water study,” *Appl. Opt.* **42**, 883-892 (2003).

16. E. J. D'Sa, and R. L. Miller, "Bio-optical properties in waters influenced by the Mississippi River during low flow conditions," *Remote Sens. Environ.* **84**, 538-549 (2003).
17. J. D. Cochran, and F.J. Kelly Jr., "Low-frequency circulation on the Texas-Louisiana continental shelf," *J. Geophys. Res.* **91**, 10645-10659 (1986).
18. C. C. Moeller, O. K. Huh, H. H. Roberts, L. E. Gumley, and W. P. Menzel, "Response of Louisiana Coastal Environments to a cold front passage," *J. Coastal Res.* **9**, 434-447 (1993).
19. W. D. Nowlin, and C. A. Parker, "Effects of a cold-air outbreak on shelf waters of the Gulf of Mexico," *J. Physical Oceanogr.* **4**, 467-486 (1974).
20. O. K. Huh, L. J. Rouse, and N.D. Walker, "Cold air outbreaks over the northwest Florida Continental shelf: Heat flux processes and hydrographic changes," *J. Geophys. Res.* **89**, 717-726 (1984).
21. E. J. D'Sa, And R. L. Miller, "Bio-optical properties of coastal waters," in *Remote sensing of aquatic coastal environments: Technologies, techniques and application*, R.L. Miller, C. Del Castillo, and B. McKee, eds. (Springer, 2005). pp. 129-155.
22. S. Maritorena, A. Morel, and B. Gentili, "Determination of the fluorescence quantum yield by oceanic phytoplankton in their natural habitat," *Appl. Opt.* **39**, 6725-6737 (2000).
23. J. R. Morrison, "In situ determination of the quantum yield of phytoplankton chlorophyll *a* fluorescence: a simple algorithm, observations, and a model," *Limnol. Oceanogr.* **46**, 618-631 (2003).

24. J. R. V. Zaneveld, J. C. Kitchen, and C. Moore, "The scattering error correction of reflecting-tube absorption meters," *Ocean Optics XII, Proc. SPIE 2258*: 44-55 (1994).
25. W. S. Pegau, D. Gray, and J. R. V. Zaneveld, "Absorption and attenuation of visible and near-infrared light in water: Dependence on temperature and salinity," *Appl. Opt.* **36**, 6035-6046 (1997).
26. J. R. V. Zaneveld, S. Pegau, and J. L. Mueller, "Volume scattering function and backscattering coefficients: instruments, characterization, field measurements, and data analysis protocols," in *Ocean optics protocols for satellite ocean color sensor validation*, NASA Tech. Memo 211621/Rev4-Vol. IV, NASA Goddard Space Flight Center, Greenbelt, MD., 2003), pp. 65-76.
27. C. D. Mobley, *Light and Water: Radiative transfer in natural water* (Academic, 1994).
28. E. Boss, W. S. Pegau, M. Lee, M. Twardowski, E. Shybanov, G. Korotaev, and F. Baratache, "Particulate backscattering ratio at LEO 15 and its use to study particle composition and distribution," *J. Geophys. Res.* **109**, C01014 - doi:10.1029/2002JC001514 (2004).
29. G. S. Fargion, and J.L. Mueller, "Ocean optics protocols for satellite ocean color sensor validation," revision 2. NASA Technical Memo. 209966, NASA Goddard Space Flight Center, Greenbelt, MD. 184 pp (2000).
30. D. A. Toole, D. A. Siegel, D. W. Menzies, M. J. Neumann, and R. C. Smith, "Remote-sensing reflectance determinations in the coastal ocean environment: impact of instrumental characteristics and environmental variability," *Appl. Opt.* **39**, 456-469 (2000).

31. H. R. Gordon, and M. Wang, "Retrieval of water-leaving radiance and aerosol optical thickness over oceans with SeaWiFS: a preliminary algorithm," App. Opt. **33**, 443-452 (1994).
32. D. A. Siegel, M. Wang, S. Maritorena, and W. Robinson, "Atmospheric correction of satellite ocean color imagery: The black pixel assumption," App. Opt. **39**, 3582-3591.
33. S. W. Wright, S. W. Jeffrey, R. F. C. Mantoura, C. A. Llewellyn, T. Bjornland, D. Repeta, and N. Welschmeyer, "Improved HPLC method for the analysis of chlorophylls and carotenoids from marine phytoplankton," Mar. Ecol. Prog. Ser. **77**, 183-196 (1991).
34. M. Kishino, M. Takahasi, N. Okami, and S. Ichimura, "Estimation of the spectral absorption coefficients of phytoplankton in the sea," Bull. Mar. Sci. **37**, 634-642 (1985).
35. B. G. Mitchell, and D. A. Kiefer, "Variability in the pigment specific fluorescence and absorption spectra in the northeastern Pacific Ocean," Deep Sea Res. Part A, **35**, 665-689 (1988).
36. E.J. D'Sa, R. G. Steward, A. Vodacek, N. V. Blough, And D. Phinney, "Optical absorption of seawater colored dissolved organic matter determined using a liquid capillary waveguide," Limnol. Oceanogr. **44**, 1142-1148 (1999).
37. R. L. Miller, M. Belz, C. E. Del Castillo, and R. Trzaska, "Determining CDOM absorption spectra in diverse aquatic environments using a multiple pathlength, liquid core waveguide system," Cont. Shelf Res. **22**, 1301-1310 (2002).
38. T. R. Parsons, Y. Maita, and C. M. Lalli. *A manual of chemical and biological methods for seawater analysis* (Pergamon, 1984).

39. A. Morel, and B. Gentili, "Diffuse reflectance of oceanic waters. III. Implication of bidirectionality for the remote-sensing problem," Appl. Opt. **35**, 4850-4862 (1996).
40. A. Morel, and B. Gentili, "Diffuse reflectance of oceanic waters. II. Bidirectional aspects," Appl. Opt. **32**, 6864-6879 (1993).
41. S.A. Garver, and D. A. Siegel, "Inherent optical property inversion of ocean color spectra and its biogeochemical interpretation. I. Time series from the Sargasso Sea," J. Geophys. Res. **102**, 18607-18625 (1997).
42. R. M. Pope, and E. S. Fry, "Absorption spectrum (380-700 nm) of pure water. II. Integrating cavity measurements," Appl. Opt. **36**, 8710-8723 (1997).
43. A. Bricaud, M. Babin, A. Morel, and H. Claustre, "Variability in the chlorophyll-*a* specific absorption coefficients of natural phytoplankton: Analysis and parameterization," J. Geophys. Res. **103**, 13321-13332 (1995).
44. H. D. Sosik, and B. G. Mitchell, "Light absorption by phytoplankton, photosynthetic pigments and detritus in the California Current System," Deep-Sea Res. **44**, 1717-1748 (1995).
45. Z. P. Lee, K. L. Carder, C. D. Mobley, R. G. Steward, and J.S. Patch, "Hyperspectral remote sensing for shallow waters. I. An analytical model," Appl. Opt. **37**, 6329-6338 (1998).
46. R. A. Reynolds, D. Stramski, and B. G. Mitchell, "A chlorophyll-dependent semi analytical reflectance model derived from field measurements of absorption and backscattering coefficients within the Southern Ocean," J. Geophys. Res. **106**, 7125-7138 (2001).

47. A. Morel, "Optical properties of pure water and sea water," in *Optical aspects of oceanography*, N.G. Gerlov and E. Steemann-Nielsen, eds. (Academic, London, 1974) pp. 1-24.
48. T. J. Petzold, "Volume scattering functions for selected ocean waters," Scripps Institute of Oceanography, San Diego. Ref. 72-78, 79 pp., (1972).
49. R. W. Gould, R. A. Arnone, and P. M. Martinolich, "Spectral dependence of the scattering coefficient in case 1 and case 2 waters," *Appl. Opt.* **38**, 2377-2383 (1999).
50. A. Morel, and S. Maritorena, "Bio-optical properties of oceanic waters: A reappraisal," *J. Geophys. Res.* **106**, 7163-7180 (2001).
51. G. L. Hitchcock, W. J. Wiseman Jr., W. C. Boicourt, A. J. Mariano, N. Walker, T. A. Nelsen, and E. Ryan, "Property fields in an effluent plume of the Mississippi River," *J. Mar. Sys.* **12**, 109-126 (1997).
52. N. D. Walker, "Satellite assessment of Mississippi River plume variability: causes and predictability," *Remote Sens. Environ.* **58**, 21-35 (1996).
53. S. P. Dinnel, S. P., and W. J. Wiseman Jr., "Fresh water on the Louisiana and Texas shelf," *Cont. Shelf Res.* **6**, 765-784 (1986).
54. R. E. Green, H. M. Sosik, and R. J. Olson, "Contributions of phytoplankton and other particles to inherent optical properties in New England continental shelf waters," *Limnol. Oceanogr.* **48**, 2377-2391.
55. M. S. Twardowski, E. Boss, J. B. Macdonald, W. S. Pegau, A. H. Barnard, and R. V. Zaneveld, "A model for estimating bulk refractive index from the optical backscattering ratio and the implications for understanding particle composition in Case I and II waters," *J. Geophys. Res.* **106**, 14129-14142 (2001).

56. J. M. Sullivan, M. S. Twardowski, P. L. Donaghay, and S. A. Freeman, "Use of optical scattering to discriminate particle types in coastal waters," *App. Opt.* **44**, 1667-1680 (2005).
57. K. L. Carder, R. G. Steward, G. R. Harvey, and P. B. Ortner, "Marine humic and fulvic acids: Their effects on remote sensing of ocean chlorophyll," *Limnol. Oceanogr.* **34**, 68-81 (1989).
58. M. Babin, J.-C. Therriault, L. Legendre, and A. Condal, "Variations in the specific absorption coefficient for natural phytoplankton assemblages: Impact on estimates of primary production," *Limnol. Oceanogr.* **38**, 15-177 (1993).
59. M. Babin, M., D. Stramski, G. M. Ferrari, H. Claustre, A. Bricaud, G. Obolenski, and N. Hoepffner, "Variations in the light absorption coefficients of phytoplankton, nonalgal particles, and dissolved organic matter in coastal waters around Europe," *J. Geophys. Res.* **108**, 3211- doi:10.1029/2001JC000882 (2003).
60. C. S. Roesler, M. J. Perry, and K. L. Carder, "Modeling in situ phytoplankton absorption from total absorption spectra in productive inland marine waters," *Limnol. Oceanogr.* **34**, 1510-1523 (1989).
61. S. Sathyendranath, L. Prieur, and A. Morel, "A three-component model of ocean color and its application to remote sensing of phytoplankton pigments in coastal waters," *Intl. J. Remote Sens.* **10**, 1373-1394 (1989).
62. H. Loisel, and A. Morel, "Non-isotropy of the upward-radiance field in typical coastal case 2 waters," *Intl. J. Rem. Sens.* **22**, 275-295.
63. G. C. Chang, T. D. Dickey, C. D. Mobley, E. Boss, and W. S. Pegau, "Toward closure of upwelling radiance in coastal waters," *Appl. Opt.* **42**, 1574-1582.

64. R. E. Green, and H. M. Sosik, "Analysis of apparent optical properties and ocean color models using measurements of seawater constituents in New England continental shelf surface waters," J. Geophys. Res. **109**, C03026-
doi:10.1029/2003JC001997 (2004).
65. V. Wright, "The seasonal dynamics of colored dissolved organic matter in the Mississippi River plume and Northern Gulf of Mexico," M.S. Thesis, University of Southern Mississippi, 68p.

FIGURE LEGENDS

Fig. 1. Study area showing the locations of the 12 stations (plus signs) occupied during a research cruise 17 - 26 March 2002 in the Northern Gulf of Mexico. Also shown are the three passes of the Mississippi River delta including the Southwest (SW) Pass through which most of the River water is discharged. Atmospheric data for this study was acquired from the NOAA C-MAN station located at the tip of the SW Pass.

Fig. 2. Atmospheric and Mississippi River water discharge conditions during the study period in March 2002. (a) Wind speed and direction, and (b) pressure and air temperature recorded at the NOAA National Data Buoy Center C-MAN station (BURL1) (Fig. 1) indicated the passage of a cold front system around 22 March, 2002. (c) Mississippi River water discharge recorded at the U.S. Army Corps of Engineers monitoring station at Tarbert Landing, Mississippi.

Fig. 3. (Color) Chlorophyll concentration derived from SeaWiFS data for the study area on (a) 17, (b) 19, (c) 22 and (d) 24 March 2002. The pluses indicate the location of field observations. Clouds are masked to black.

Fig. 4. Cross-shelf transect through stations 5, 6, 7 and 8 (offshore to nearshore) conducted over a one day period on (a) 18 March and (b) 24 March 2002 showing the temporal variability in sea surface temperature (SST), salinity and Chl fluorescence

(relative fluorescence units, RFU) measured with a flow-through system onboard the R/V Pelican.

Fig. 5. Water column profiles of physical and bio-optical properties at station 6 obtained on (a, c) 18 March and (b, d) 24 March 2002. (a, b) Comparison of vertical profiles of density, Chl, and ratio of particulate backscattering to scattering $b_{bp}:b_p$, (c, d), absorption (particulate plus CDOM, and CDOM) and particulate scattering.

Fig. 6. Comparison of vertical profiles of salinity(a, f) and bio-optical properties such as Chl (b, g), absorption (particulate plus CDOM) (c, h), particulate scattering (d, i), and ratio of particulate backscattering to scattering $b_{bp}:b_p$ (e, j) for stations 2, 4, 5, 10, and 12 obtained during periods before (top panel) and after (bottom panel) the frontal passage. An additional profile at station 12 obtained on 25 March is plotted to show representative daily variation in salinity and bio-optical properties.

Fig. 7. The ratio of Chl:SPM as a function of the backscattering ratio $b_{bp}(532):b_p(532)$ for samples obtained at surface, mid-depth and bottom at the 12 stations before and after the frontal passage.

Fig. 8. Results of CDOM absorption plotted as a function of salinity and the slopes of the log-linearized absorption spectra S_{cdom} for seasonal data obtained in April and October of 2000, and March of 2002. (a) Salinity versus CDOM absorption $a_{cdom}(412)$ (m^{-1}) for discrete samples (surface, mid and bottom depths) obtained at the twelve stations during

March 2002. Data are also plotted for measurements obtained in April and October of 2000 for comparison. Solid line is the linear regression fit to all data points. (b) S_{cdom} (nm^{-1}) plotted as a function of $a_{cdom}(412)$ (m^{-1}) for April and October 2000, and March 2002.

Fig. 9. Spectral absorption properties of particulate and dissolved seawater constituents in surface samples. (a) Comparison of phytoplankton, CDOM and nonalgal particle spectral absorption coefficients (a_{ph} , a_{cdom} , and a_{nap}) at station 6 on 18 and 24 March 2002 showing the large variability in absorption properties. Pure water absorption is plotted for comparison. (b) measured versus modeled values of phytoplankton absorption at

SeaWiFS wavebands, (c) phytoplankton specific absorption spectra $a^*_{ph}(\lambda)$, (d) log-linearized absorption spectra of nonalgal particles S_{nap} (nm^{-1}), (e) ratio of absorption by non-algal particles to total particulates at 443 nm versus chlorophyll concentrations, and (f) log-linearized absorption spectra of CDOM before and after the frontal passage.

Fig. 10. Comparison of (a) phytoplankton, (b) (nonalgal particles (at 443 nm), (c) CDOM absorption (at 412 nm), and (d) suspended particulate matter (SPM) as a function of Chl (mg m^{-3}) for surface samples obtained in March 2002, and April and October 2000. Linear regressions (solid line) were determined only for March 2002 samples.

Fig. 11. (a) Normalized particulate scattering spectra as a function of wavelength (top panel), (bottom panel) average value of the normalized particulate scattering spectra of surface samples, and the average scattering spectra of Gould et al.⁴⁹ (b) Particulate backscattering b_{bp} versus particulate scattering b_p for surface waters at 532 nm, and (c)

particulate scattering $b_p(555)$ versus Chl (mg m^{-3}) for surface samples showing regression line (solid) for March 2002. Also shown for comparison are the scatter plots for measurements obtained in April and October 2000. The dashed line shows the Morel model⁵⁰ for case I waters determined at 550 nm.

Fig. 12. Remote sensing reflectance spectra R_{rs} at SeaWiFS wavebands (412, 443, 490, 510, 532, 555, and 670 nm) derived from in-water radiometric measurements (solid line, solid circle), and IOP model derived (dotted line, triangle) using Eq. 2. Also shown for comparison are the R_{rs} spectra determined from above-water measurements using the GER-1500 fiber-optic based radiometer. Also plotted are the SeaWiFS derived R_{rs} spectra using the Gordon and Wang³⁰ (diamonds), and the iterative³¹ (squares) atmospheric correction algorithms for the nearshore stations 10, 7 and 8 obtained within 3 hours of satellite pass. Right panel shows the % difference between the IOP model and in-water radiometric derived estimates of R_{rs} .

Fig. 13. Comparison between the ratios of remote sensing reflectance R_{rs} determined from measurements with above-water and in-water radiometers at same locations in April 2000 and March 2002 for (a) $R_{rs}(490)/R_{rs}(555)$, and (b) $R_{rs}(510)/R_{rs}(555)$. Results of (c) surface Chl (mg m^{-3}) plotted as a function of ratios of R_{rs} at 490 and 555 nm wavebands ($R_{rs}(490)/R_{rs}(555)$), and (d) surface CDOM absorption (m^{-1}) at 412 nm plotted as a function of R_{rs} ratio $R_{rs}(510)/R_{rs}(555)$ for April and October 2000 and March 2002. Linear regression fit (solid line) was determined using all data points.

Fig. 14. A comparison between in situ and SeaWiFS derived Chl concentrations and CDOM absorption at 412 nm for data acquired in April and October 2000, and March 2002. (a) Chl retrieved from ratios of SeaWiFS derived R_{rs} using Eq. 11, and (b) CDOM absorption (at 412 nm) retrieved from ratios of SeaWiFS derived R_{rs} using Eq. 12 .Solid line is the linear regression fit to all data points.

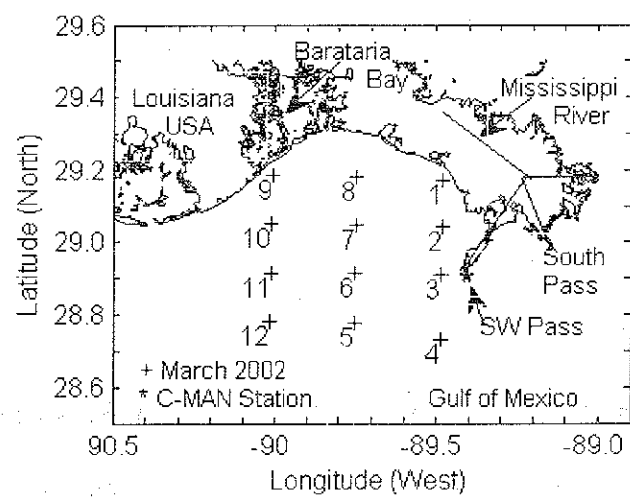


Fig. 1.

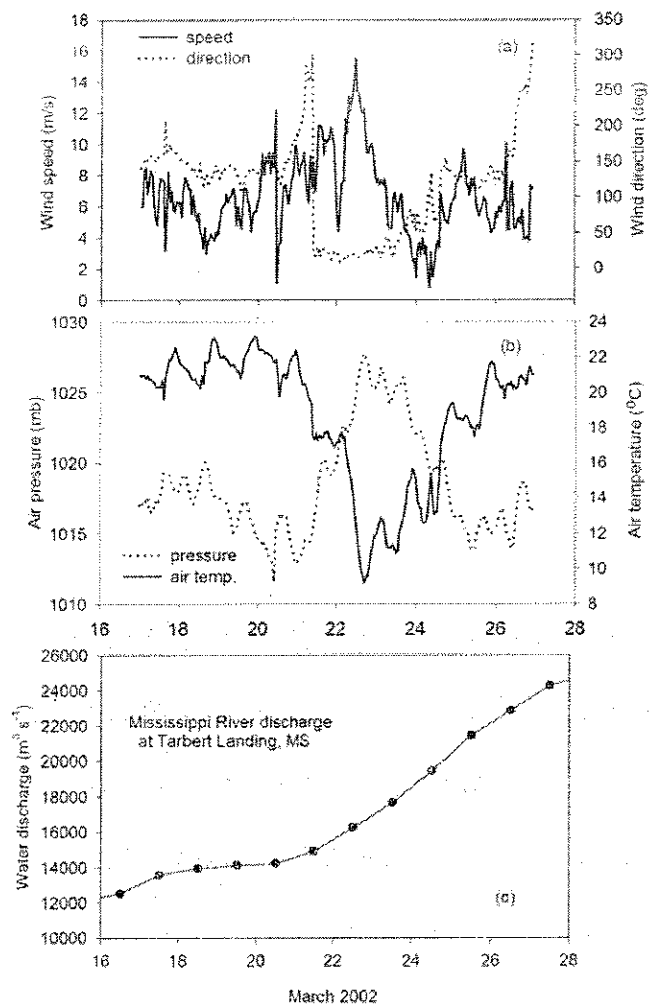


Fig 2.

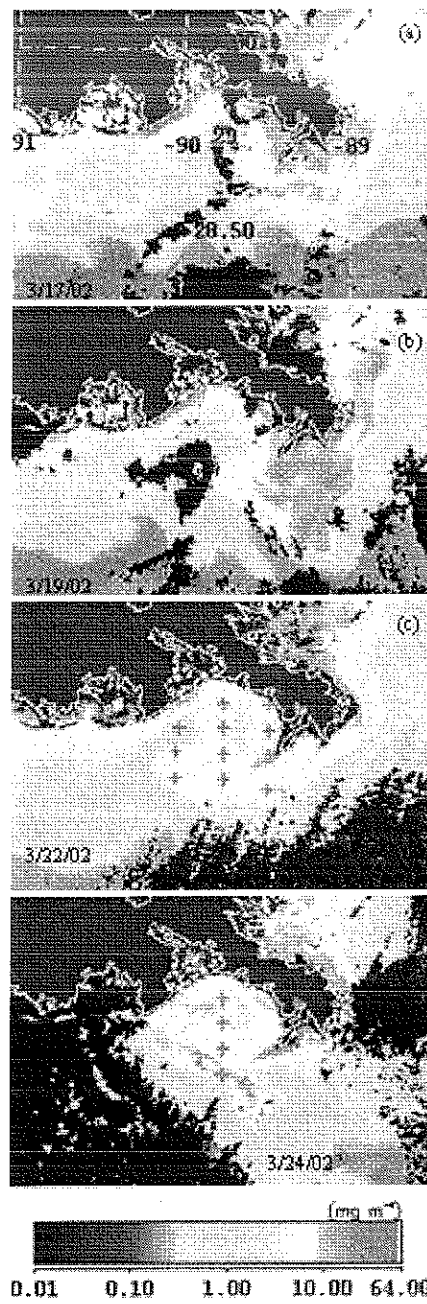


Fig. 3.

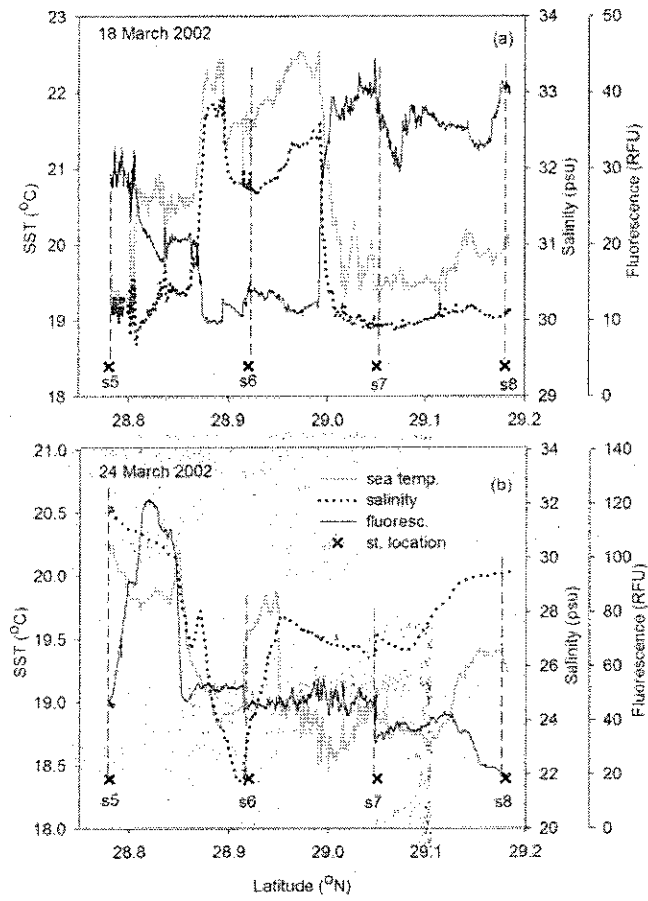


Fig. 4.

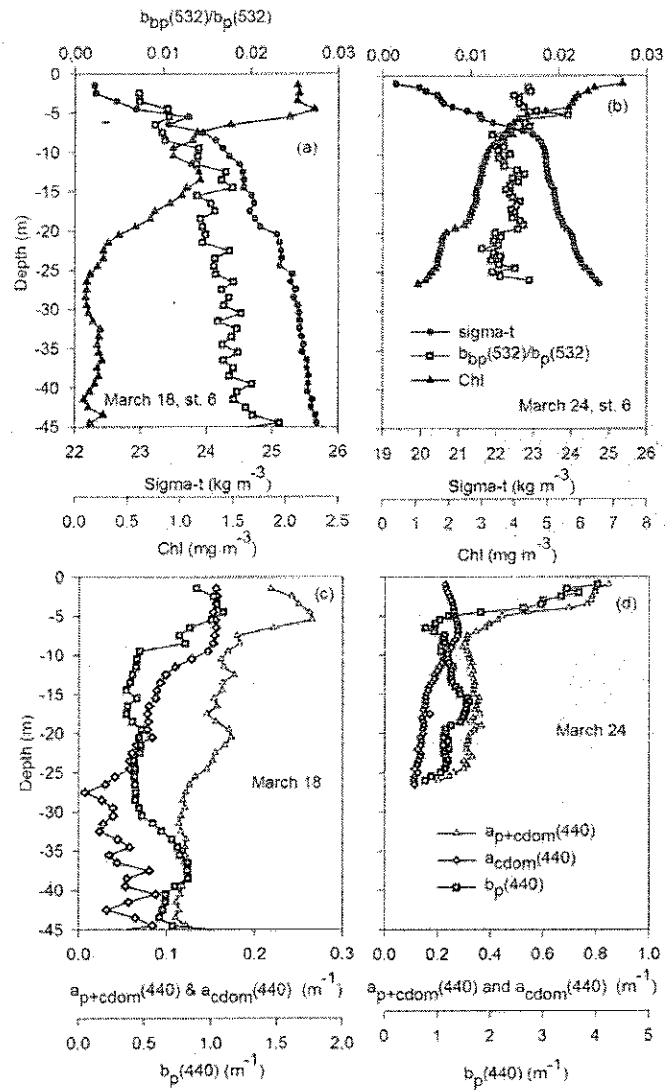


Fig. 5.

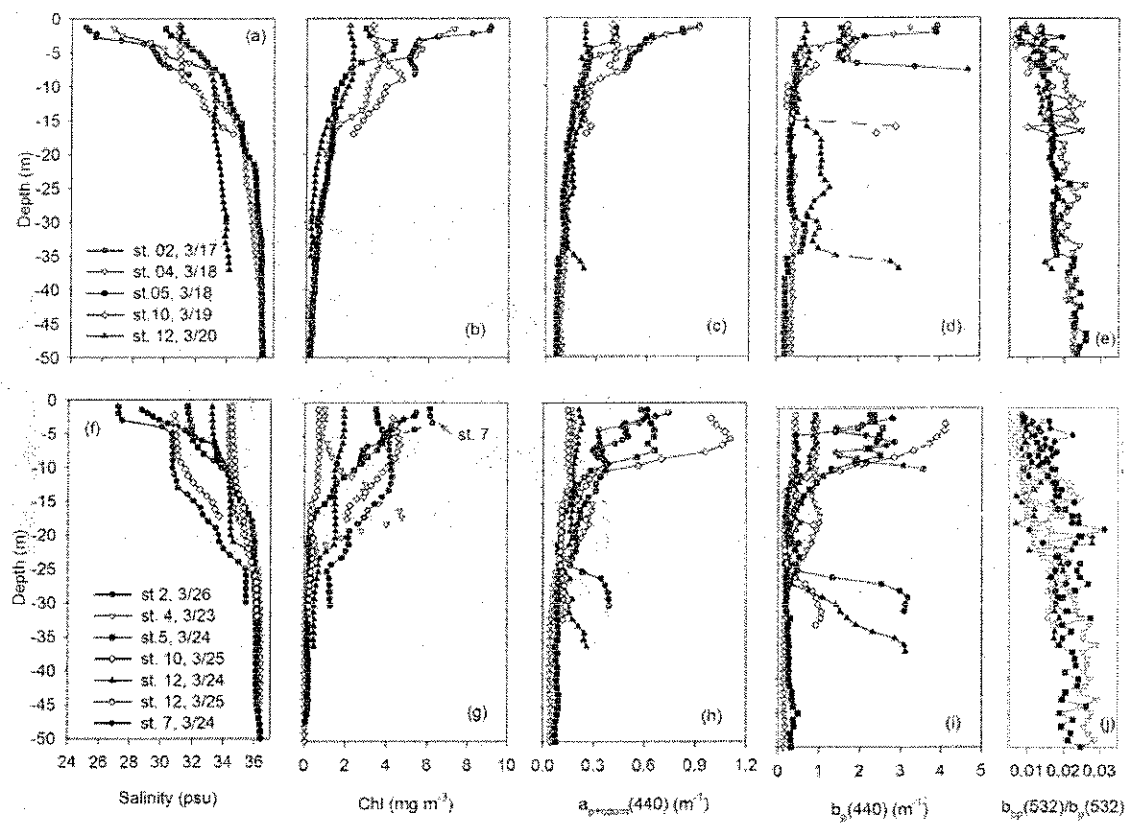


Fig. 6.

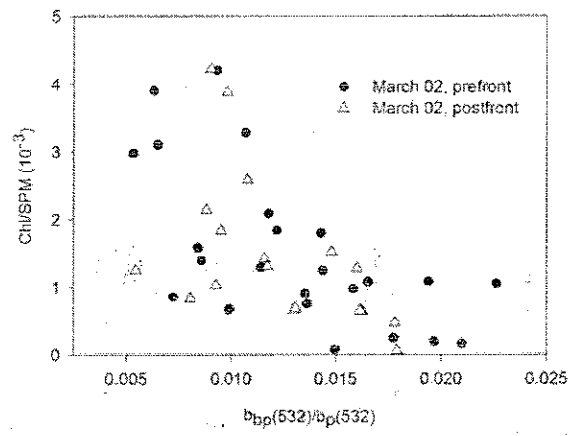


Fig. 7.

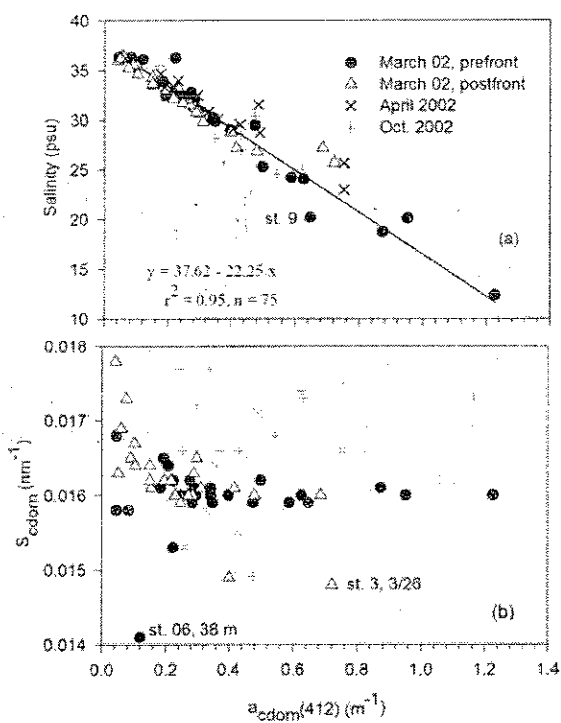


Fig. 8.

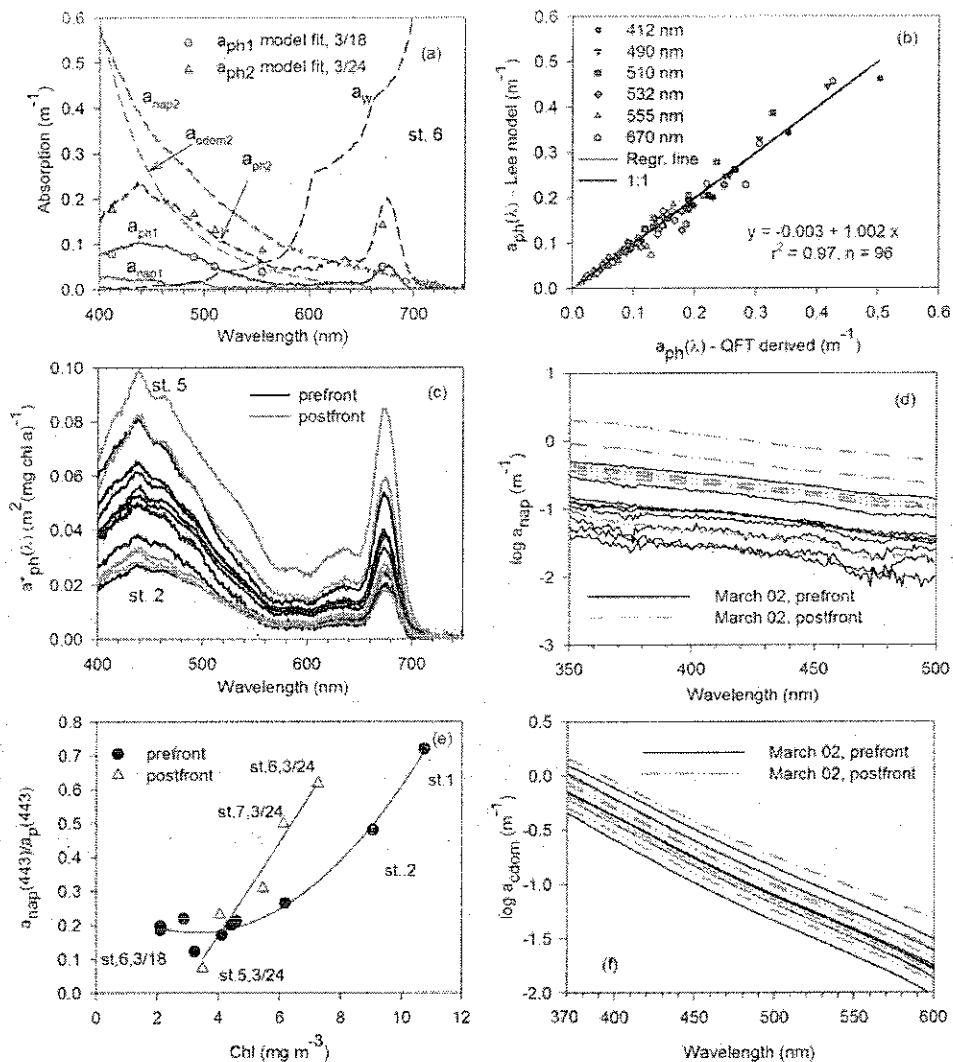


Fig 9.

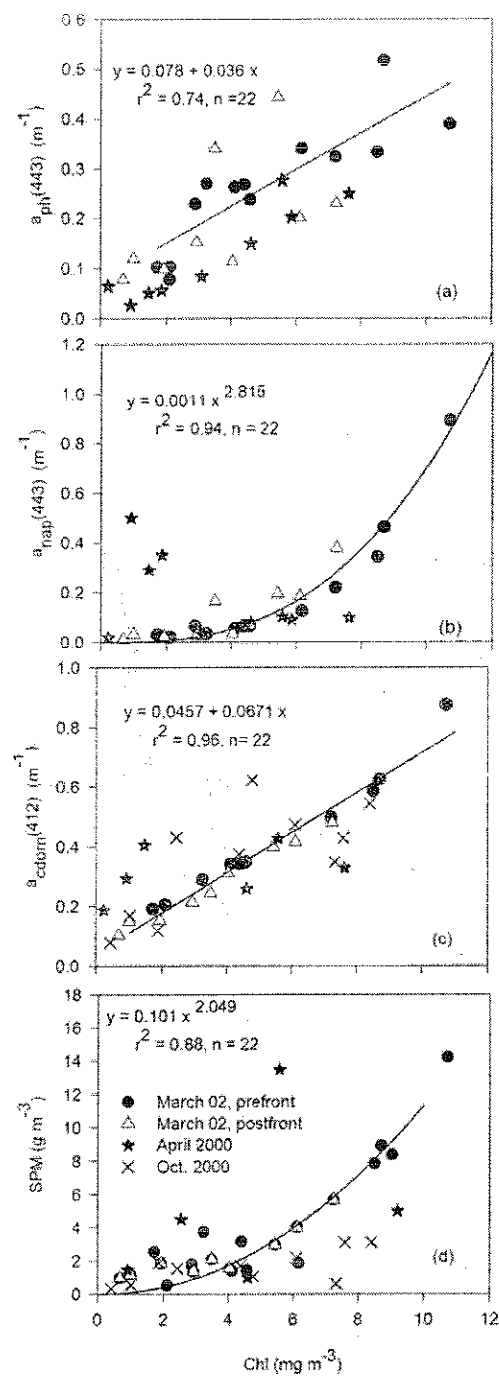


Fig. 10.

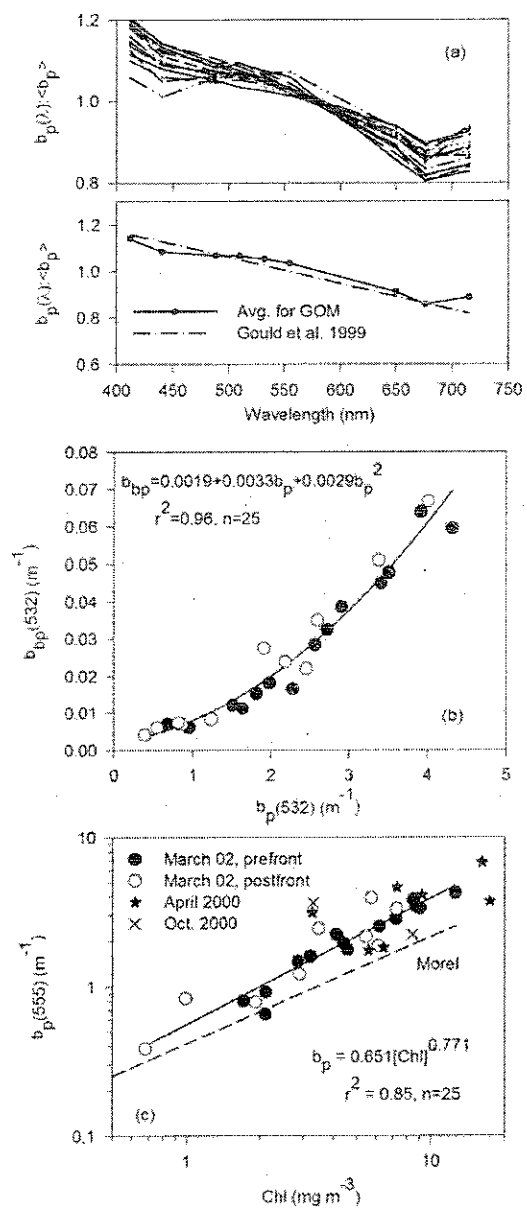


Fig. 11.

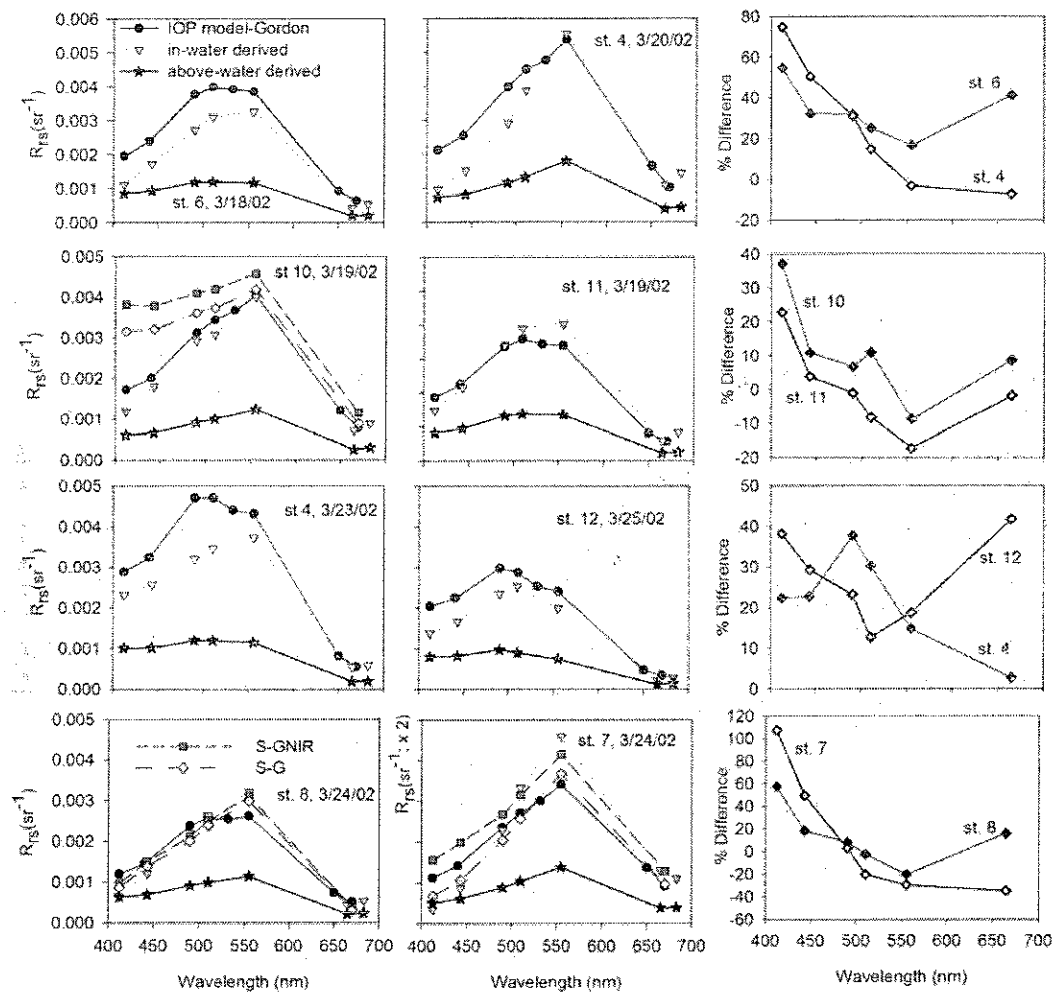


Fig. 12.

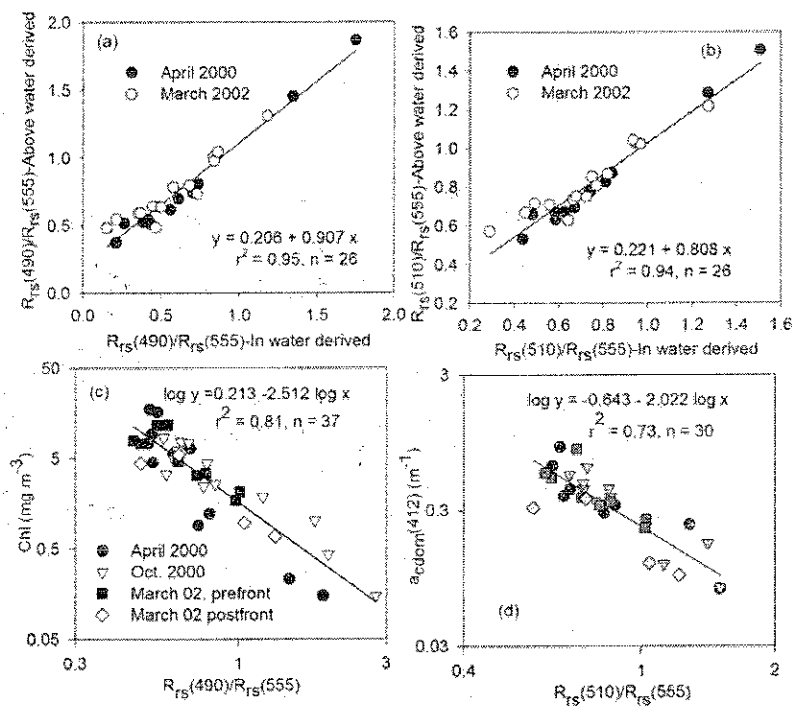


Fig. 13.

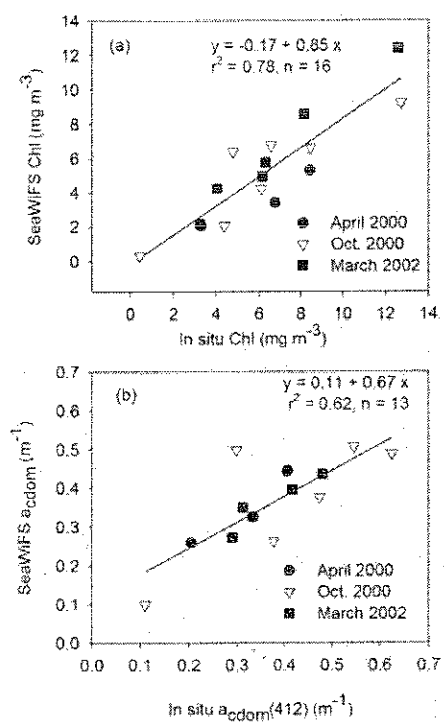


Fig. 14.

Table 1. Surface (0 to 3 m) physical and bio-optical properties for stations 8, 7, 6, and 5 (mid-transect) and stations 4, and 12 (offshore) for the periods 17-21 and 23-26 (brackets) March 2002 corresponding to the pre- and post frontal passage. Station 6 is marked in bold to highlight the station with the largest relative change in optical properties.

Properties	St. 8	St. 7	St. 6	St 5	St 12	St. 4
Temp. ($^{\circ}\text{C}$)	19.84 (19.02)	18.83 (18.82)	20.46 (19.04)	19.23 (19.60)	21.30 (19.73)	19.94 (20.36)
Salinity (psu)	30.26 (29.85)	30.08 (27.18)	31.89 (27.56)	30.28 (31.70)	31.00 (33.56)	29.89 (34.35)
Sigma-t (kg m^{-3})	21.19 (21.08)	21.31 (19.14)	22.29 (19.95)	21.30 (22.35)	21.37 (23.49)	20.88 (24.16)
Chl (mg m^{-3})	4.40 (4.04)	4.11 (6.11)	2.11 (7.24)	2.86 (3.48)	2.10 (1.92)	4.57 (0.99)
SPM (mg l^{-1})	3.15 (1.56)	1.38 (4.02)	0.54 (5.67)	1.80 (2.10)	0.50 (1.86)	1.47 (1.19)
$a_{\text{ph}}(443)$ (m^{-1})	0.268 (0.114)	0.263 (0.202)	0.103 (0.230)	0.229 (0.340)	0.078 (0.099)	0.238 (0.120)
$a_{\text{nap}}(443)$ (m^{-1})	0.067 (0.034)	0.056 (0.184)	0.022 (0.379)	0.066 (0.166)	0.020 (0.023)	0.065 (0.032)
$a_{\text{cdom}}(443)$ (m^{-1})	0.201 (0.276)	0.204 (0.213)	0.155 (0.231)	0.208 (0.277)	0.123 (0.093)	0.210 (0.073)
% $a_{\text{cdom}}(443)$	37.1 (64.0)	38.5 (35.2)	54.2 (27.2)	40.8 (35.1)	54.1 (42.1)	40.4 (31.4)
% $a_{\text{ph}}(443)$	49.4 (26.4)	49.7 (33.3)	36.7 (27.2)	44.9 (43.1)	34.3 (44.7)	45.7 (51.7)
$b_{\text{p}}(443)$ (m^{-1})	2.076 (0.556)	3.049 (2.260)	1.017 (3.440)	1.581 (2.336)	0.684 (0.872)	2.303 (0.902)
$b_{\text{p}}(532)$ (m^{-1})	1.955 (0.534)	2.970 (2.094)	0.962 (3.350)	1.498 (2.412)	0.683 (0.849)	2.220 (0.828)
$b_{\text{pp}}(532)$ (m^{-1})	0.0167 (0.006)	0.0199 (0.031)	0.0069 (0.056)	0.0125 (0.021)	0.0063 (0.007)	0.0255 (0.007)
$b_{\text{pp}}(532)/b_{\text{p}}(532)$	0.0085 (0.011)	0.0067 (0.014)	0.0072 (0.017)	0.0083 (0.009)	0.009 (0.008)	0.0114 (0.008)